

STRANGE PARTICLES PRODUCED
BY π^+ p COLLISIONS AT 10.3 GeV/c

M. Goddard

A Thesis Submitted in Partial Fulfillment
of the Requirements for the Degree of

Master of Science
(Physics)

UNIVERSITY OF TORONTO

1975

Acknowledgements

It takes a large number of people and a lot of time to convert one and a half million pictures into useful information. For the Toronto data I would like to thank Mrs. Sheila Maggs and her team of measurers and scanners. I am grateful to Bruce Bolin and Peter Kahan for their programming help. I am indebted to all those who helped edit the strange particle events. Special thanks go to my supervisor Tony Key for his helpful advice. Thanks go to Rosslyn Nanton for her speedy typing of the manuscript.

INTRODUCTION

This thesis is based on an experiment done at the Stanford Linear Accelerator Center in the spring of 1972. The experiment was a collaboration between Toronto and a group from Brookhaven National Laboratory. Approximately half a million (three-view) pictures were taken of π^+p interactions in the 82-inch hydrogen bubble chamber at a beam momentum of 10.3 GeV/c. The film was divided between Toronto and Brookhaven and analyzed separately.

Particle Physics attempts to understand the "basic" particles of nature and the manner in which they interact. High energy collisions provide the most common way of observing these interactions and producing new particles. This experiment was designed to examine the production mechanisms of well known resonances and to search for boson resonances with masses in the region 2-3 Gev. The statistics are larger than any previous π^+p bubble chamber experiment making our results (hopefully) more reliable and less ambiguous than others.

This thesis is a discussion of the experimental setup, film and data analysis (Toronto only) of the events where strange particles are produced. As an example of the physics analysis of the data, an examination of $\pi^+p \rightarrow K^{*+}(890) \Sigma^+(1385)$ (combined Toronto and Brookhaven data) is presented.

EXPERIMENTAL SETUP

BUBBLE CHAMBERS

The basic bubble chamber consists of a closed vessel containing a liquid at a temperature above its normal boiling point but under sufficient pressure to prevent boiling. By suddenly expanding the liquid through its saturation vapour pressure we obtain a super-heated liquid. The liquid is now in a metastable state, needing only localized energy to create the liquid vapour interface and precipitate boiling. The passage of a charged particle will ionize electrons in the liquid and these then deposit enough concentrated energy to provide nucleation centers for boiling to start. The bubble chamber then becomes a detector of charged particles.

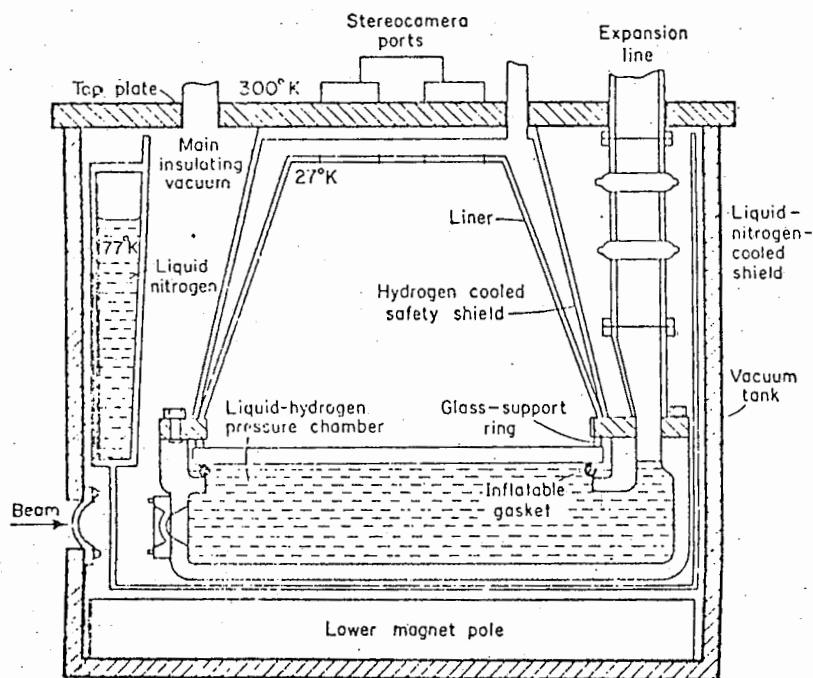
Occasionally a (non-coulomb) scattering off the liquid nucleus takes place and we have both a detector and target for high energy interactions.

By using liquid hydrogen as the bubble chamber liquid we get an unambiguous proton target, with low coulomb scattering and tracks which will be long enough (before secondary scattering) for good momentum determination.

When the chamber is sensitive, a short (microsecond) beam pulse from the accelerator enters. The bubbles are created almost instantaneously (about 10^{-10} sec.) and then there is a relatively slow (msec.) growth to photographable size (about 300 microns). Note that the short beam duration, compared to bubble growth time, ensures that all photographed bubbles are at essentially

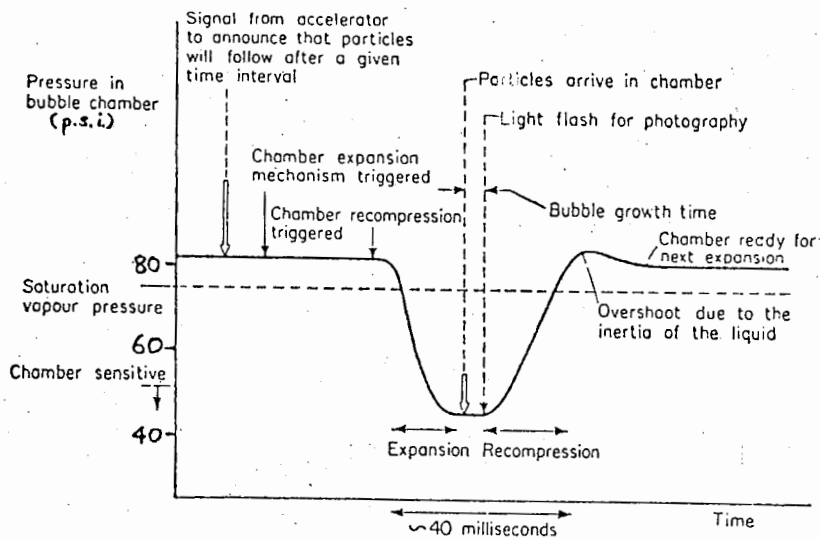
the same size. At the appropriate instant the chamber is illuminated and the pictures taken. Recompression is started as soon as possible and the bubbles are squeezed out of existence. The chamber is then ready for another cycle. The whole process takes about a second.

It is crucial that no temperature gradients be created in the liquid, because these will set up convection currents in the hydrogen and distort or move the tracks. Furthermore the bubble growth rate and bubble density are sensitive functions of the expanded pressure and temperature. The bubble size and density for beam tracks should be constant throughout the chamber operation. This sets tolerances on the pressure and temperature of ± 0.01 °K and $\pm 1/2$ p.s.i. The bubble density must be high enough to make vertices well defined and yet not so high as to obliterate all the low velocity tracks. A compromise at about 15 bubbles/cm is usually chosen.



SKETCH PLAN OF A BUBBLE CHAMBER

from Bradner (1960)



from Henderson (197

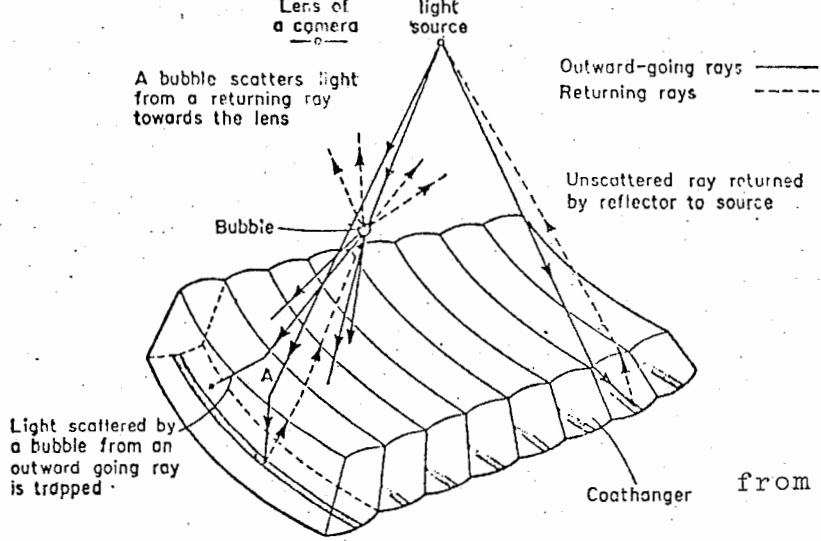
The sequence of operations in a bubble chamber.

THE 82-INCH BUBBLE CHAMBER

Originally designed (in 1958) for use with the Berkeley 6 GeV Bevatron in investigating the properties of the newly discovered strange particles, it was enlarged and moved to SLAC in 1968.

The top of the chamber is 5" thick optical glass, tilted approximately 6° from the horizontal. This permits stray bubbles and other impurities to roll out of the viewing area. Each interaction is photographed by three cameras situated at the vertices of a right-angled triangle. To avoid multiple track images a retrodirective illumination system is used. With this system only light scattered by the bubbles from behind is imaged in the camera and all other light is absorbed. The tracks therefore appear white on a black background. (see next page).

Etched into the underside of the top glass are 19 fiducial marks (of which only 15 are visible in the pictures). There are also 10 body fiducials attached to the sides of the chamber and 6 fiducials on the bottom. These fiducials are necessary in the spatial reconstruction of the tracks.



Strip of aluminium reflector on the base of each coathanger
 All coathanger surfaces, except top surface and the reflecting strip, blackened to absorb light

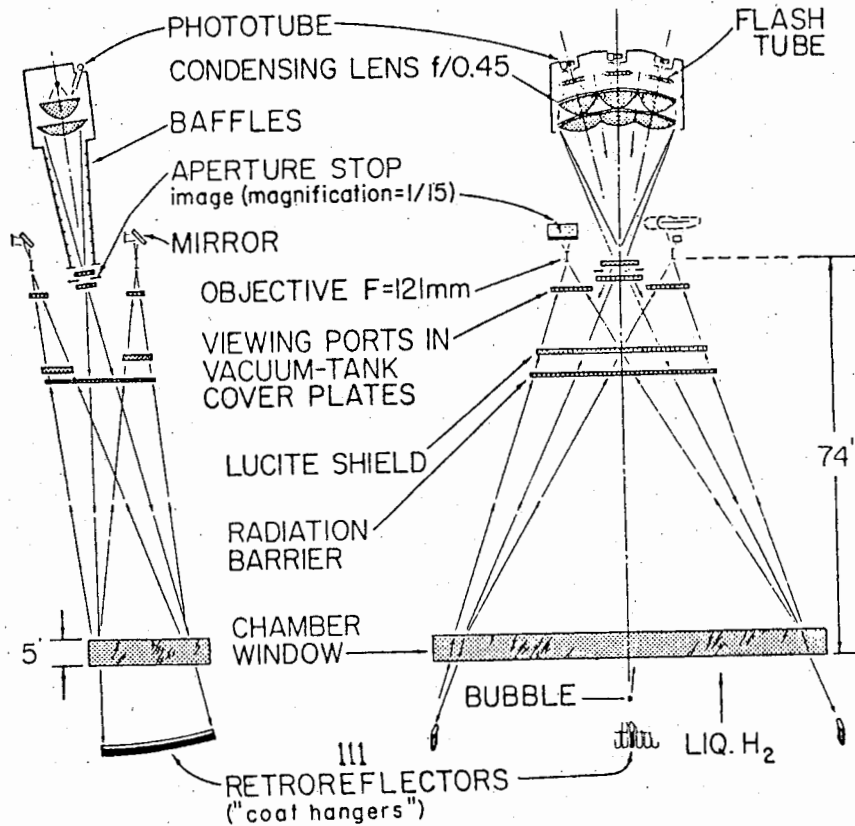
The coathanger system.

This highly diagrammatic sketch shows the principle of retrodirective illumination.

The ray of light concerned in photographing the bubble leaves the source and is bent at A, the surface of a transparent plastic 'coathanger'. The coathangers are based on a spherical surface centred at the light source. The ray, being radially directed, is reflected at the polished aluminium strip, and on leaving the plastic heads for the bubble where it is scattered strongly only in the forward direction. Some of this scattered light enters the cameras to form the photographic images.

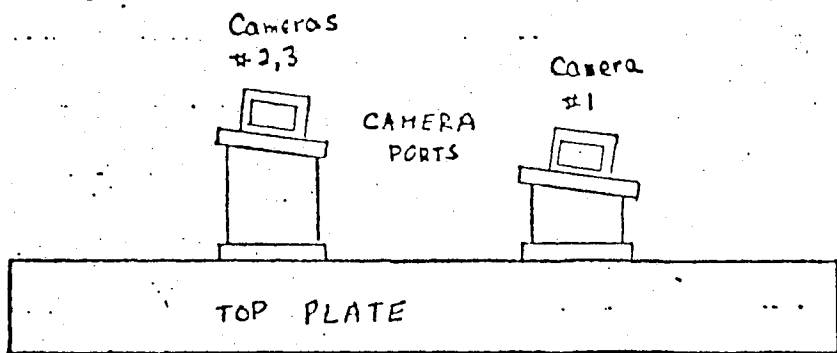
A ray of light heading straight from the source to the bubble scatters light strongly only towards the coathangers, which they enter in a non-radial direction and therefore miss the aluminium strip and fall on absorbing surfaces.

If a simple spherical reflecting surface is used, images both of the bubble and of its reflection in the mirror appear on the photograph.

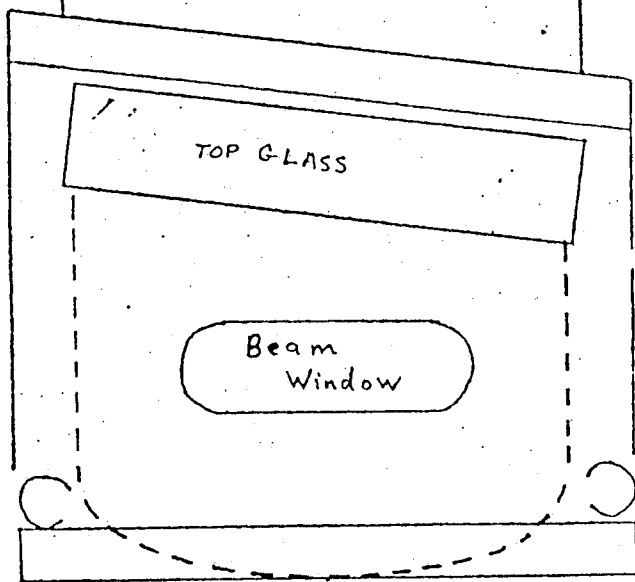
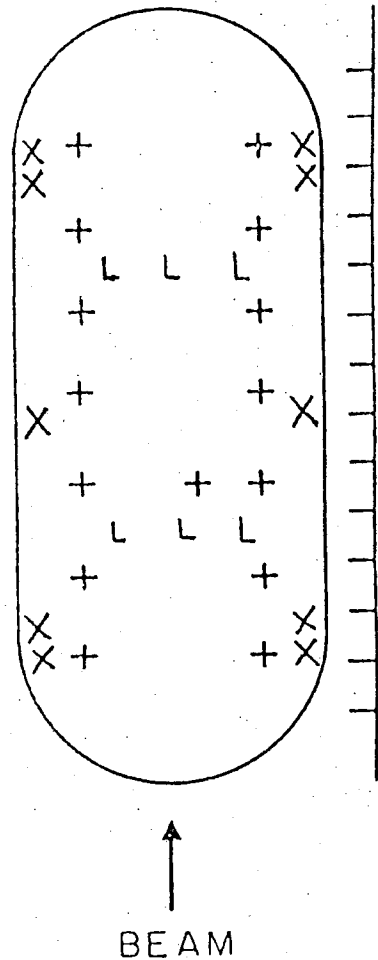


Optical system of the 82-inch chamber.

82-INCH BUBBLE CHAMBER



fiducials
 X - body fiducials
 + - glass fiducials
 L - coat-hanger fiducials



(Rake side)

Beam into page

(a) Vertical View

(b) 82" bubble chamber see from top (camera side)

Shape	Racetrack
Beam plane dimensions	82" x 20"
Depth	17"
Approximate visible volume	500 liters
Orientation	Window on top at approximately 6° to horizontal
Maximum pulse rate	2 pps
Illumination	Coathangers - dark field
Entrance beam window	4" x 13.5"; .06" S. S.
Exit beam window	None
Magnetic field	1.7 Tesla (1.55 Tesla presently)
Expansion	Hydraulic, bellows

Optical System

Light source	3 xenon flashtubes EG&G, No. FX51, nominally 100 J/pulse/tube
Filter	None
Condenser	2 element f .45
Vacuum tank ports	1 illuminating, 1 viewing/polaroid, 3 camera (2.5" thick, Nd=1.46)
Cooldown tank ports	None
Main window	Thickness, 5.118" Refractive index, Nd=1.52 Glass type BK7 No. of fiducials, 19

Optical System

Chamber body
fiducials (wall
mounted)

82" HBC

Fiducial rake along one side and 5 fiducials on
either side of chamber approximately .25" below
glass. Two beam entrance fiducials in beam
plane (7.6" below glass).

Retrodirector

Piston mounted (moving); Coathangers

Cameras3 track, 35 mm

Three separate cameras mounted on common
plate with common drive. Film, 35 mm Type II
perforated, EK No. 2474, 1200' rolls. Lenses
90 mm Schneider Super Angulon, mounted on 3
cameras of 20" nominally square. Film ad-
vance 22 perforations (4.12") per camera.
Nominal fiducial demagnification is 20:1.

BEAM

The Stanford Linear Accelerator produces a 1.5 microsecond pulse of 19 GeV electrons 360 times a second. Some of these pulses are diverted to become the primary beam for the 82-inch bubble chamber. This primary beam is focused onto a beryllium target producing many secondary particles with a wide spectrum of energies. From all of the particles with different momenta entering the secondary beam we must present to the bubble chamber only π^+ 's with well defined momenta. The important elements in the primary and secondary beam are described below.

A momentum bite (10.5 GeV/c $\pm 2.5\%$) is selected by dispersing the beam (D1) and then adjusting the collimator (F2). An RF separator selects the π^+ 's, so that out of F2 comes a separated π^+ beam with a 5% momentum bite. The beam is then focused on the chamber and pictures are taken if the number of particles entering is between certain pre-determined limits. In this experiment, to obtain uncluttered pictures and yet be certain of obtaining a reasonable number of events, the mean number of tracks entering the chamber was about 12.

Main Constituents of Beam Line (refer to diagram on Page 9)

Primary electron beam:-

B60 - bends electrons up by 0.3° and steers them onto target.

Q60-61 - quadrupole doublet which focuses electron beam on the target

B61 - steers beam onto target in horizontal plane

Target - beryllium, 0.25 inches square and 1 foot long, suspended by thin wires from an electrically insulated cage

ZnS Screen - monitors beam hitting target

Dump - stops the beam after it passes through target.

Secondary Beam:-

6Q1-2 - quadrupole doublet which focuses the target on F1 (horizontal magnification $\frac{1}{2}$, vertical magnification 2)

6D1 - disperses beam for momentum bite selection at F1.

F1 - iron collimator with $\frac{5}{8}$ inch square opening, this chooses momentum bite to be 5%.

6Q3-4 - focuses F1 onto F2

6D2 - removes dispersion from beam

6D2.1 - bends the beam upward

RF Separator - separates out π^+ 's

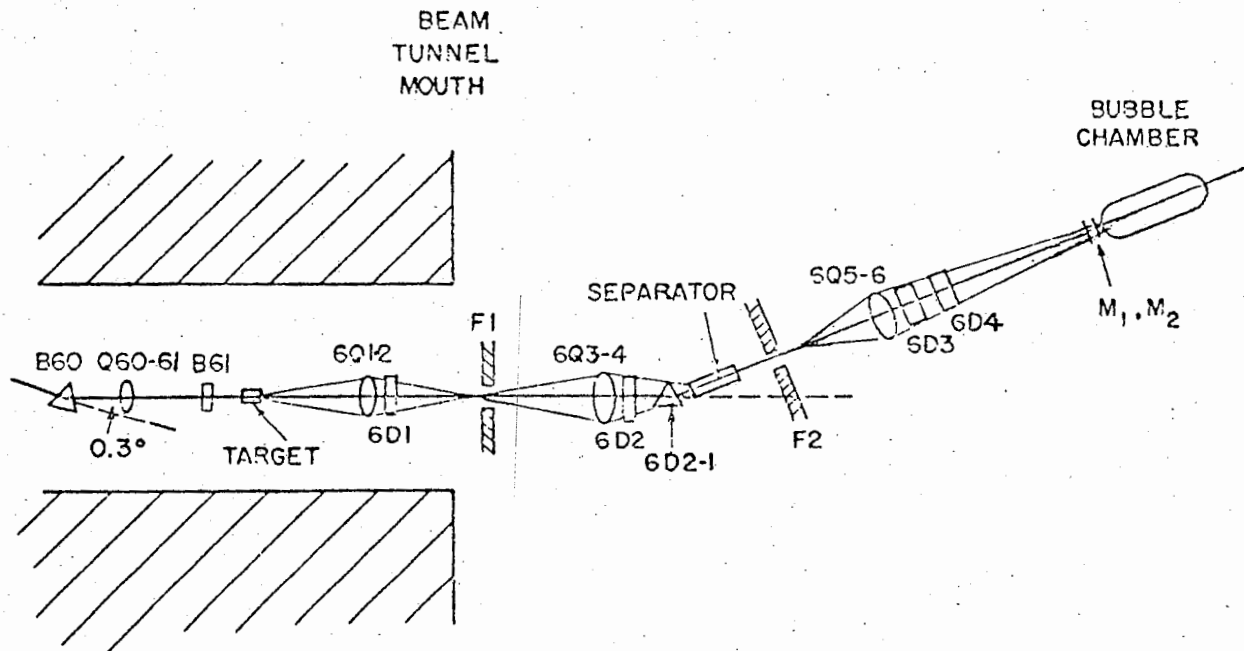
F2 - 3 foot long iron collimator, with vertical opening of $\frac{5}{8}$ inch and horizontal opening of $\frac{1}{2}$ inch.

6Q5-6 - quadrupole doublet provides parallel beam through 6D3-4

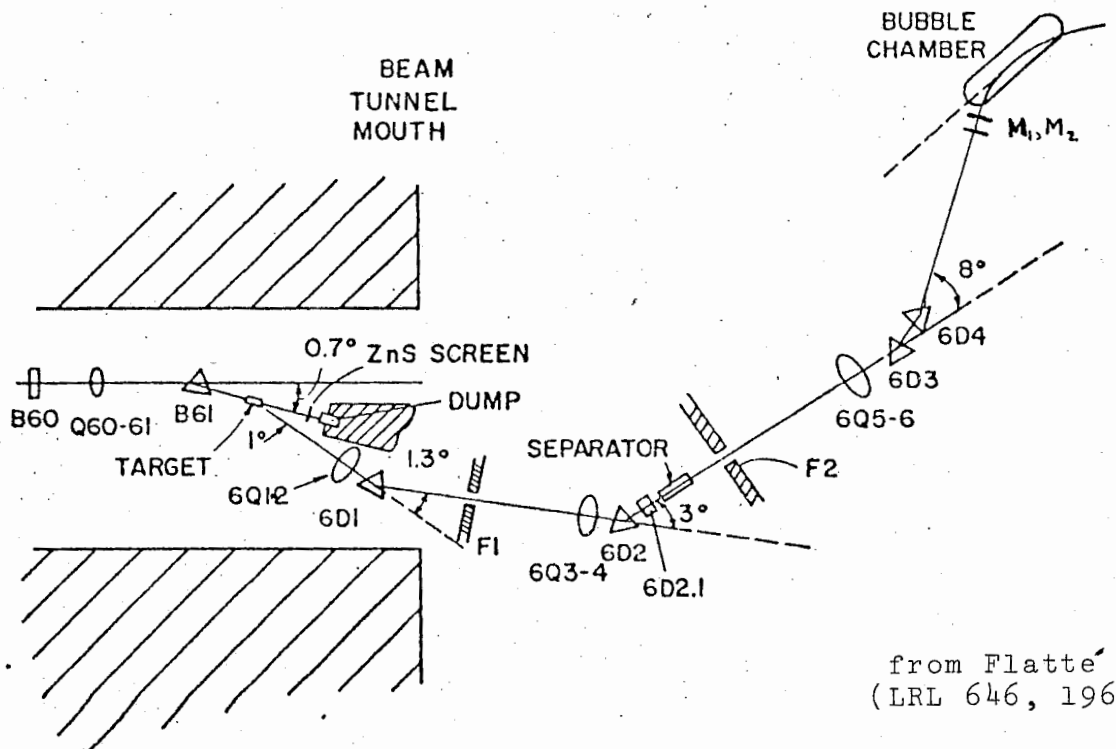
6D3-4 - provides dispersion in the bubble chamber of 1% per 2 inches

Bubble Chamber - beam enters through a thin stainless steel window.

VERTICAL VIEW OF BEAM



HORIZONTAL VIEW OF BEAM



from Flatte
(LRL 646, 1968)

DATA REDUCTION

OPTICS

Before the bubble chamber tracks can be reconstructed in space from their images on film, the camera positions and lens distortions must be calculated. These parameters can be determined given enough chamber fiducials whose relative positions are well known.

The positions of the 15 visible glass fiducials and 2 bottom fiducials for each of the three cameras were measured on several frames of the film. These, along with their accurately known positions in the chamber, were used by the programme Python (Zoll (1965)) to find the lens distortions and camera positions for each view. Comparison of the relative positions of the glass fiducials with their image on film yielded the distortion coefficients. The demagnifications of all fiducials and the positions of the bottom fiducials were used to determine the camera positions.

It is assumed that the lens distortions map the real film images onto an ideal film plane (i.e. film images we would have if the lens were a pinhole with no distortions). The transformation is assumed to be of the form:

$$\begin{pmatrix} x' \\ y' \end{pmatrix} = (1 + \alpha x + \beta y + \gamma R^2 + \delta R^4) \begin{pmatrix} X \\ Y \end{pmatrix} + \begin{pmatrix} \epsilon R^2 \\ \kappa R^2 \end{pmatrix}$$

$R^2 = x^2 + y^2$; $\alpha, \beta, \gamma, \delta, \epsilon, \kappa$, = distortion coefficients

$$\begin{pmatrix} x \\ y \end{pmatrix} = \text{real film images} \quad \begin{pmatrix} x' \\ y' \end{pmatrix} = \text{ideal film images}$$

For each camera Python provides us with the coefficients α , β , α , δ , ϵ , κ , and the camera's position. These allow the measured points along a track (on film) to be transformed to the ideal plane where they are connected to the reconstructed tracks in three-dimensional space by simple pinhole optics. This makes the track reconstruction problem much simpler.

STRANGE PARTICLES

The strange particles are strange because they are produced strongly (in times of order 10^{-23} sec) but decay only weakly (and sometimes electromagnetically). This is "explained" by introducing an internal quantum number (called strangeness) which is conserved in strong (and electromagnetic), but violated in weak interactions. This predicts that there are no open strong decay channels which conserve strangeness, thus forcing the strange particles to decay by strangeness-violating weak interactions (Nishijima (1954)).

Therefore the signature of a strange particle is a charged or neutral decay several centimeters from the initial interaction. A neutral decay (called a vee) appears in the chamber as two oppositely charged tracks originating from a common point with no visible incident track. A charged decay (called a kink)

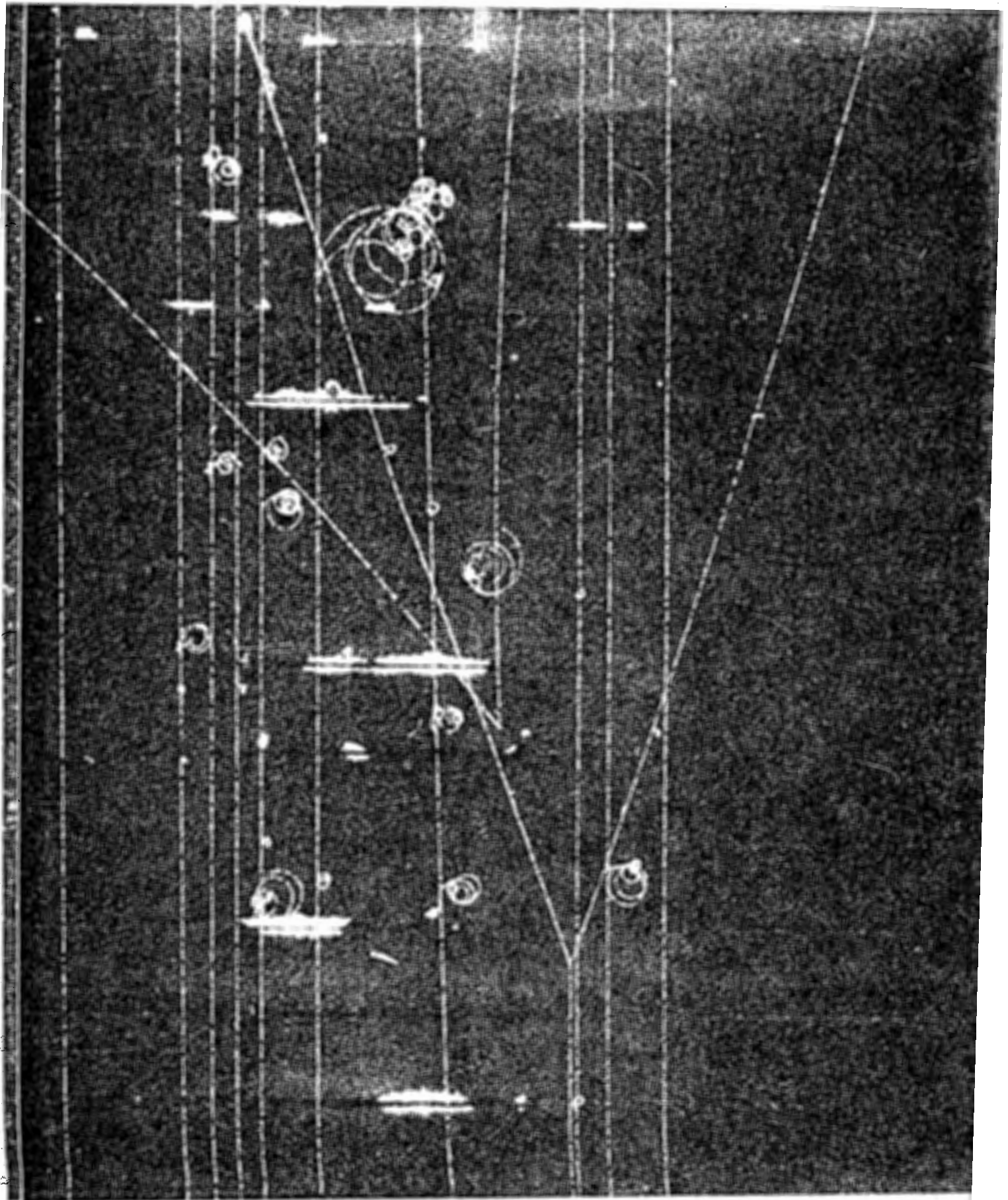
is a track which abruptly changes its direction (because of momentum carried off by an unseen neutral particle). An interaction with a vee and a kink is pictured on page 13. (Unfortunately the "kink" track is really a proton elastically scattering off of a hydrogen nucleus. The recoil proton is going down at about 50° to the plane of the photograph and stops after about 1 cm. It is therefore almost impossible to see. The "vee" is however a genuine $K^0 \rightarrow \pi^+ \pi^-$).

SCANNING

All of the film has to be visually scanned to select events of interest for measurement. In this case we are interested only in events with strange particles in the final state. Therefore, those events with vees or kinks are sent on for measuring. In addition any tracks that obviously stop in the bubble chamber are noted so that they may be treated differently in the reconstruction. The efficiency for spotting strange particle events is expected to be greater than 95%.

MEASUREMENT

The tracks are measured by magnifying the 35mm film approximately 20 times and projecting them onto a screen. An operator then manually moves the point to be measured to



PROPERTIES OF STRANGE PARTICLES

Particle	Mass (MeV)	$c\tau$ (cm)	Most Common Decay Products	Strangeness
K^{\pm}	493.707	370.8	$\mu^{\pm}\nu$ 64% $\pi^{\pm}\pi^0$ 21%	± 1
K^0, \bar{K}^0	497.70	2.66(K_S^0) 1553(K_L^0)	$\pi^+\pi^-$ 69% $\pi^0\pi^0$ 21%	+1, -1
Λ	1115.60	7.73	$p\pi^-$ 64% $n\pi^0$ 36%	-1
Σ^+	1189.37	2.40	$p\pi^0$ 52% $n\pi^+$ 48%	-1
Σ^-	1197.35	4.44	$n\pi^-$	-1
Σ^0	1192.48	$<10^{-14}$	$\Lambda\gamma$	-1

From: Particle Properties (April 1974)

coincide with a reference mark on the screen and the coordinates of this point are transmitted to the on-line computer. An average of seven points are measured along each track. To provide orientation for the event, four fiducials are also measured. The accuracy with which a point can be measured on these machines is about 2 microns on the film which corresponds to 0.04 millimeters in real space. The measuring rate is 2.8 events (three views) per hour.

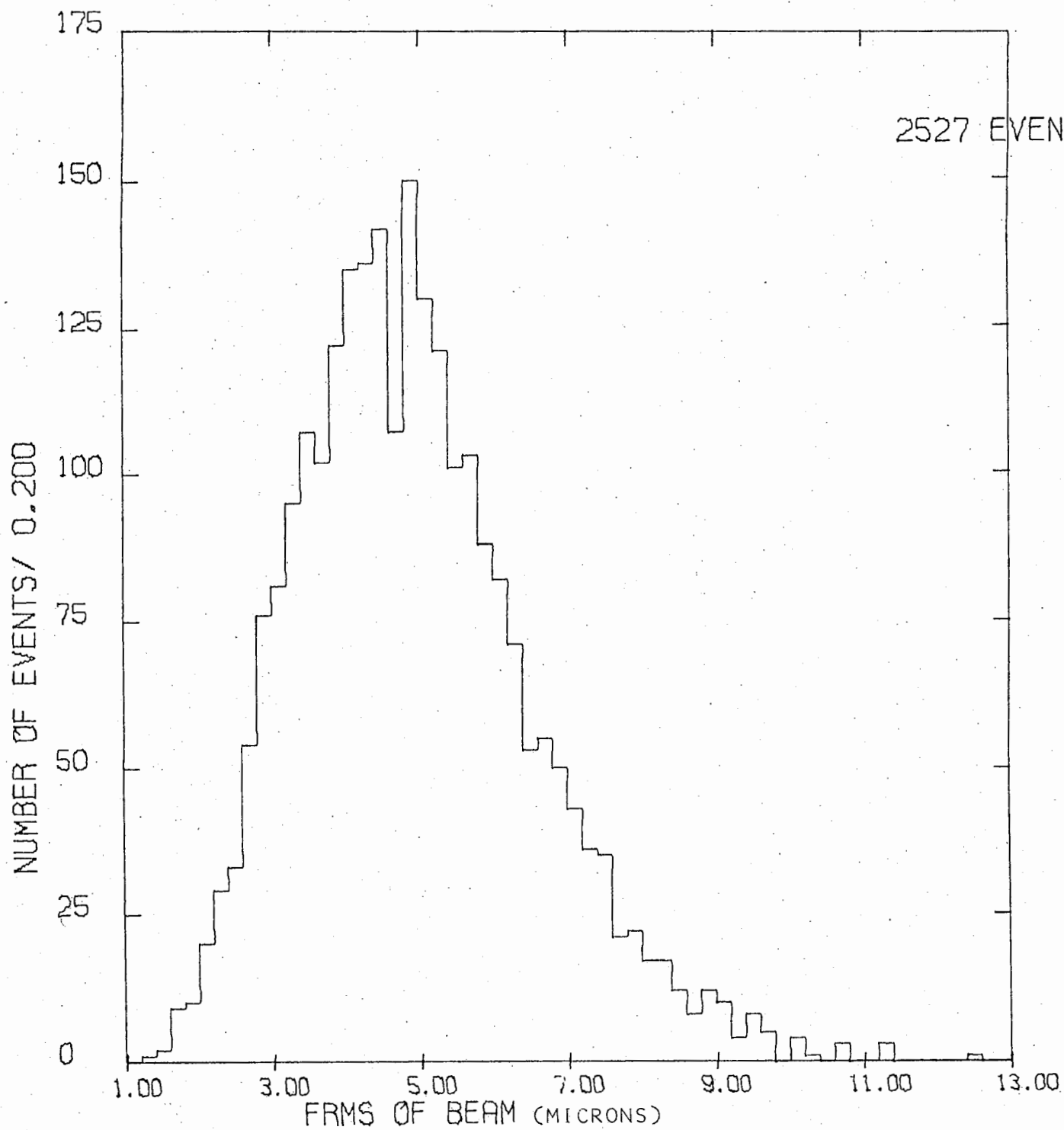
SPATIAL RECONSTRUCTION

The track measurements are reconstructed in space from their film images in the three views using the programme TVGP (Three View Geometry Programme) (Solmitz, 1965). The distortions are removed from the measurements using the parameters determined by Python so that the measured point and its image on the film are connected by simple pinhole optics.

Given three views of the same event and knowing the positions of the three cameras, TVGP reconstructs the track in the bubble chamber. The general shape is taken to be a helix, with variations in the magnetic field along the track and ionization loss folded in. The parameters of the curve are varied until its projection onto the film minimizes the sum of the squares of the distances from the measured points (FRMS). The errors in the curve parameters are obtained from

the FRMS plus a "setting error" which represents the unknown errors (from optics, bubble chamber turbulence, measuring machines, etc.). On the following page is a histogram of the FRMS for a number of beam tracks. The horizontal scale is microns on the film. The FRMS includes a small contribution from coulomb scattering (about 0.3 microns for beam tracks) which causes the tracks to deviate from the fitted helix. Values for the FRMS of a few microns mean that TVGP is able to reconstruct the points fairly well and this is a reflection of good optical constants.

Therefore at this stage the complete geometry of the event is known. It remains only to make correct mass assignments to each track.



KINEMATIC RECONSTRUCTION

We characterize each event by a "topology code" which contains the number of vees, positive and negative kinks, and outgoing charged tracks. For each topology we select a set of final states (consistent with selection rules) and determine whether any, or all of these reactions are compatible with four-momentum conservation. For each topology the final states which we attempt to fit are listed on pages 23 and 24.

The TVGP output is used as input to the programme SQUAW (Dahl, 1968) which does the kinematic fitting according to our hypotheses. This is achieved by varying the (TVGP) measured values for the track parameters, those with large errors being freer to move than those with small errors. The track parameters we use are: $\vec{m} = (\phi, \tan\lambda, k = \frac{1}{p\cos\lambda})$, where λ is the dip of the track with respect to the plane of the glass, ϕ is the angular orientation in this plane and p is the momentum. These are chosen because they are most nearly Gaussian distributed (Berge, 1961). We also have an error matrix: $M_{iJ}^{-1} = (\delta m_i \delta m_J)_{ave}$, where $M_{ii}^{-1} = \sigma_i^2$ and off-diagonal elements are the correlations between variables of one track. We assume, however, that there are no inter-track correlations.

At each vertex we have the constraint equations of energy-momentum conservation, which can be expressed in the form:

$F_\lambda(\vec{x}) = 0$ (where \vec{x} are the fitted track variables). To "fit"

the reaction we must minimize the quantity:

$$\chi^2 = \sum_{i,J} (x-m)_i M_{iJ} (x-m)_J \equiv (\vec{x}-\vec{m})^T M(\vec{x}-\vec{m})$$

subject to the above constraints. An equivalent, but in general easier, problem is to minimize:

$$N = \chi^2 + \sum_{\lambda} 2\alpha_{\lambda} F_{\lambda}(\vec{x}) \equiv \chi^2 + 2\vec{F} \cdot \vec{\alpha}$$

where $\vec{\alpha}$ is a vector of Lagrange multipliers. N must be minimized with respect to $\vec{\alpha}$ and \vec{x} . Therefore

$$\frac{1}{2} \frac{\delta N}{\delta \vec{x}} = 0 = M(\vec{x}-\vec{m}) + B(\vec{m})\vec{\alpha};$$

$$B(\vec{m})_{i\lambda} = \left(\frac{\delta f_{\lambda}}{\delta x_i} \right)_{\vec{x}=\vec{m}}$$

therefore

$$\vec{x} = \vec{m} - M^{-1} B(\vec{m})\vec{\alpha} \quad (1)$$

Since F is in general non-linear and B is a function of \vec{x} we must use an iterative procedure. Start the iteration by expanding $\vec{F}(\vec{x})$ around an approximation for \vec{x} , which we initially take as \vec{m} . Therefore

$$\vec{F}(\vec{x}) = \vec{F}(\vec{m}) + B^T(\vec{m})(\vec{x}-\vec{m}) = 0 \quad (2)$$

(1) in (2)

$$\vec{\alpha} = [B^T M B]^{-1} \vec{F}(\vec{m}) \quad (3)$$

(3) in (1) leads to a new value for \vec{x} . This is only approximate, since we expanded \vec{F} only to first order. We use this value for \vec{x} as our new approximation in (2). We continue the iteration until the constraints are satisfied and χ^2 is at a minimum. Specifically we finish if:

$$(1) \quad \sum_{\lambda} |F_{\lambda}(\vec{x})| < 0.015 \text{ MeV}$$

$$(2) \quad |\Delta\chi^2| < 0.075$$

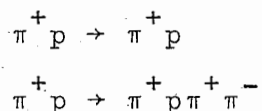
The errors on the fitted parameters are less than those on the measured and in general have inter-track correlations.

If the hypothesis to be fitted contains an unseen neutral then effectively the number of constraints is reduced since the unmeasured variables must be calculated using some of the constraint equations. Take as an example the event with a vee and a kink on page 13, at the vee vertex the only quantity unknown is k of the strange neutral (since we assume it is produced at the main vertex, we know its angles, but not its momentum). This leaves three constraints at this vertex (3-C fit). At the kink vertex there is one neutral completely missing, so we have 1 constraint at this vertex. The primary vertex now has 4 constraints and the overall constraint class for this fit is 8.

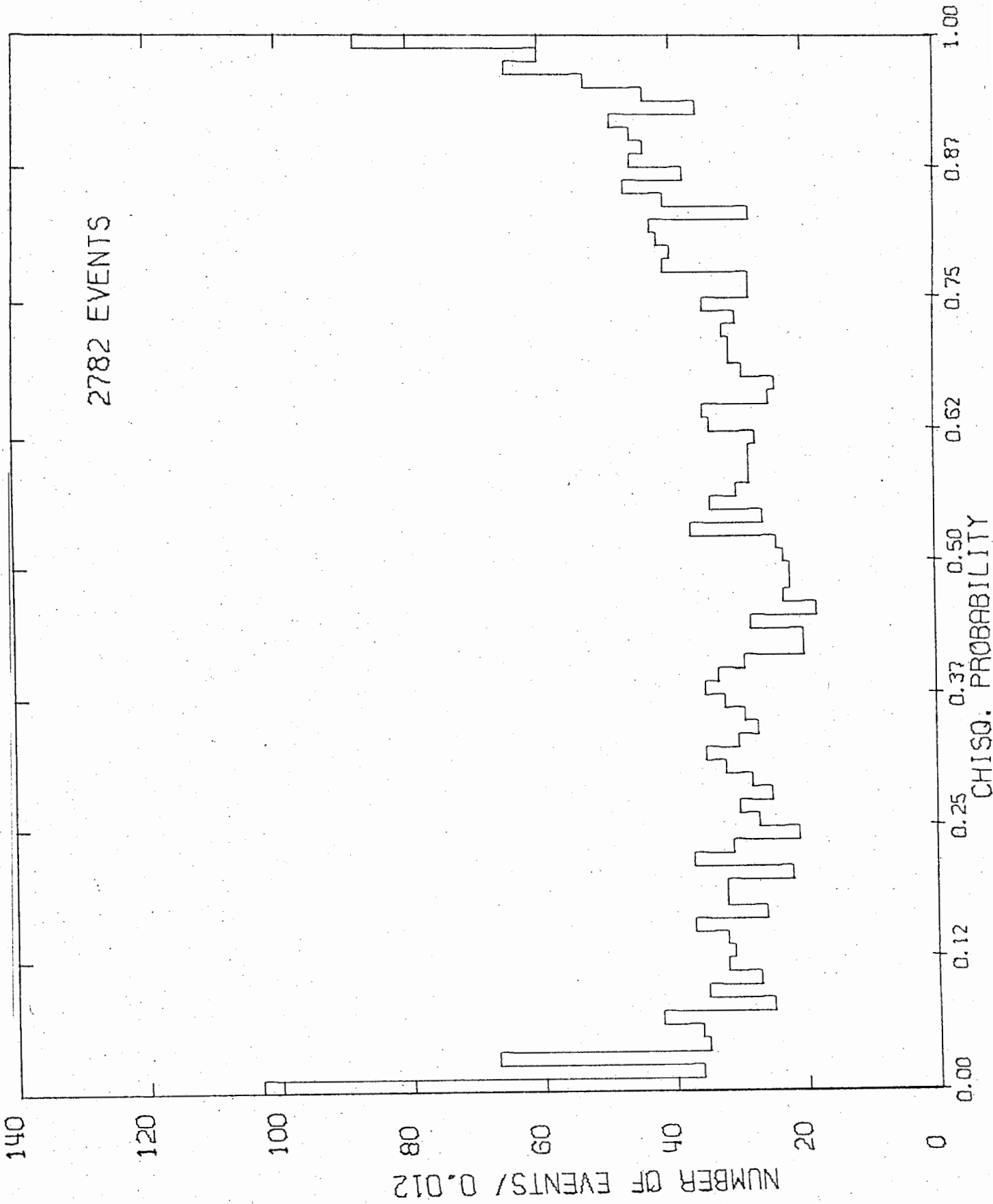
If the track parameters are normally distributed then for each fit the quantity:

$$\chi^2 = (\vec{x} - \vec{m})^T M (\vec{x} - \vec{m})$$

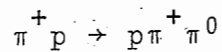
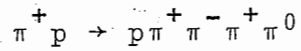
has a chi-square distribution with the number of degrees of freedom equal to the number of fit constraints. This gives us a measure of the likelihood that the fit is correct. SQUAW rejected all fits with $P(\chi^2) < 0.001 \%$. The chi-square probability distribution for a sample of non-strange events (types 4000 and 2000) which fitted the following (4-C) hypotheses:



is pictured on page 21. For correct error assignments and fitting



procedure we expect the chi-square probability distribution to be flat. It very often happens in bubble chamber experiments that the correct distribution is not attained (Rosenfeld (1963)). This is probably due to poorly known effects such as turbulence and optical distortion which make error estimates very unreliable. For our distribution the peak at low probability is probably due to badly measured events or events which are really



FINAL STATES WITH TWO STRANGE PARTICLES

Topology X101*(x≥4)	NDF	Topology X200*(x≥2)	NDF	Topology X010*(x≥2)	NDF
<u>p</u> <u>K</u> ⁻ <u>K</u> ⁰ π ⁺ π ⁺	8	pπ ⁺ <u>K</u> ⁰ <u>K</u> ⁰	10	<u>Σ</u> ⁺ (<u>K</u> ⁰)π ⁺	2
<u>p</u> <u>K</u> ⁻ <u>K</u> ⁰ π ⁺ π ⁺ (π ⁰)	5	pπ ⁺ <u>K</u> ⁰ <u>K</u> ⁰ (π ⁰)	7	<u>Σ</u> ⁺ <u>K</u> ⁺	5
(n) <u>K</u> ⁻ <u>K</u> ⁰ π ⁺ π ⁺ π ⁺	5	(n) <u>K</u> ⁰ <u>K</u> ⁰ π ⁺ π ⁺	7	<u>Σ</u> ⁺ <u>K</u> ⁺ (π ⁰)	2
<u>Σ</u> ⁻ <u>K</u> ⁰ π ⁺ π ⁺ π ⁺	8	<u>Σ</u> ⁰ <u>K</u> ⁰ π ⁺ π ⁺	8	<u>K</u> ⁺ (Λ)π ⁺	2
<u>Σ</u> ⁻ <u>K</u> ⁰ π ⁺ π ⁺ π ⁺ (π ⁰)	5	<u>Λ</u> <u>K</u> ⁰ π ⁺ π ⁺	10	<u>K</u> ⁺ (<u>Σ</u> ⁰)π ⁺	2
		<u>Λ</u> <u>K</u> ⁰ π ⁺ π ⁺ (π ⁰)	7	<u>K</u> ⁺ (<u>K</u> ⁰)p	2
				<u>K</u> ⁺ <u>K</u> ⁻ pπ ⁺	5
				<u>K</u> ⁺ <u>K</u> ⁻ pπ ⁺ (π ⁰)	2
				<u>K</u> ⁺ <u>K</u> ⁻ (n)π ⁺ π ⁺	2

*Topology Code = XVPN

X = number of charged tracks at main vertex
V = number of vees
P, N = number of positive, negative kinks

On this page and the following are listed the final states with two strange particles that we try to fit in SQUAW. A particle in parentheses indicates that it escapes detection and its presence is only inferred from the fitted four-momenta. Strange particles that are underlined are seen to decay in the bubble chamber according to one of the following schemes.

<u>Σ</u> ⁺ →	pπ ⁰ nπ ⁺	<u>K</u> ⁺ →	π ⁺ π ⁰ μ ⁺ ν	<u>Λ</u> →	pπ ⁻		
<u>Σ</u> ⁻ →	nπ ⁻	<u>K</u> ⁻ →	π ⁻ π ⁰ μ ⁻ ν	<u>K</u> ⁰ →	π ⁺ π ⁻	<u>Σ</u> ⁰ →	<u>Λ</u> γ ↓ →pπ ⁻

FINAL STATES WITH TWO STRANGE PARTICLES

Topology X100*(x≥2)	NDF	Topology X110*(x≥2)	NDF	Topology X001*(x≥4)	NDF
$p\bar{K}^+ \bar{K}^0$	7	$p\bar{K}^+ \bar{K}^0$	8	$\Sigma^-(K^0)\pi^+\pi^+\pi^+$	2
$p\bar{K}^+ \bar{K}^0(\pi^0)$	4	$p\bar{K}^+ \bar{K}^0(\pi^0)$	5	$(n)\bar{K}^- K^+ \pi^+ \pi^+$	2
$p\pi^+ \bar{K}^0(K^0)$	4	$\Sigma^+ \bar{K}^0 \pi^+$	8	$p\bar{K}^- K^+ \pi^+$	5
$(n)K^+ \bar{K}^0 \pi^+$	4	$\Sigma^+ \bar{K}^0 \pi^+(\pi^0)$	5	$p\bar{K}^- K^+ \pi^+(\pi^0)$	2
$\Lambda K^+ \pi^+(\pi^0)$	4	$(n)\bar{K}^+ \bar{K}^0 \pi^+$	5	$\Sigma^- K^+ \pi^+ \pi^+$	5
$\Lambda K^+ \pi^+$	7	$\Lambda \bar{K}^+ \pi^+$	8	$\Sigma^- K^+ \pi^+ \pi^+(\pi^0)$	2
$\Lambda(K^0)\pi^+ \pi^+$	4	$\Lambda \bar{K}^+ \pi^+(\pi^0)$	5	$\bar{K}^-(K^0)p\pi^+ \pi^+$	2
$(\Lambda)\bar{K}^0 \pi^+ \pi^+$	4	$\Sigma^0 \bar{K}^+ \pi^+$	6		
$(\Sigma^0)\bar{K}^0 \pi^+ \pi^+$	4				
$\Sigma^0 K^+ \pi^+$	5	Topology X020*(x 2)	NDF	Topology X011*(x 4)	NDF
$p\bar{K}^- \bar{K}^0 \pi^+ \pi^+(x54)$	7	$\Sigma^+ \bar{K}^+$	5	$\Sigma^- \bar{K}^+ \pi^+ \pi^+$	5
$p\bar{K}^- \bar{K}^0 \pi^+ \pi^+(\pi^0)(x54)$	4	$\Sigma^+ \bar{K}^+(\pi^0)$	2	$\Sigma^- \bar{K}^+ \pi^+ \pi^+(\pi^0)$	2
$(n)K^- \bar{K}^0 \pi^+ \pi^+ \pi^+(x54)$	4			$\bar{K}^- \bar{K}^+ p\pi^+$	5
				$\bar{K}^- \bar{K}^+ p\pi^+(\pi^0)$	2
				$\bar{K}^- \bar{K}^+(n)\pi^+ \pi^+$	2

*Topology Code = XVPN

X = number of charged tracks at main vertex

V = number of vees

P, N = number of positive, negative kinks

Fit Selection

Each event was examined to try and reduce the number of multiple fits. By looking at bubble density (which is proportional to $1/\beta^2$) it was possible to rule out certain mass assignments and therefore reject some SQUAW fits. Of the remaining fits, we kept those with the highest constraint class and rejected the others (unless that left us only with fits which had $P(\chi^2) < 0.1\%$ in which case we also kept fits in the next lowest class).

It can sometimes happen that a vee is a $\gamma \rightarrow e^+e^-$ instead of a neutral strange particle decay. To catch these events we tried to fit all vees to $\gamma \rightarrow e^+e^-$. If the attempt was successful and there was no other vee or kink, we rejected it as a non-strange event. If however, it was an event which could still have strange particles (i.e. another vee or a kink) we assumed the γ was produced from $\pi^0 \rightarrow \gamma\gamma$ or $\Sigma^0 \rightarrow \Lambda\gamma$ and attempted fits with π^0 or Σ^0 in the final state.

Similarly a proton scatter $p+p \rightarrow p+p$ with a slow recoil proton that stops after about a centimeter can appear as a kink in a track. A pion decay $\pi^+ \rightarrow \mu^+ + \nu$ will also occasionally masquerade as a strange particle decaying. These possibilities were looked for and when found the event was either discarded as non-strange or further fits were attempted.

Those events which failed to reconstruct for no obvious reason were sent back to be remeasured.

SYSTEMATICS

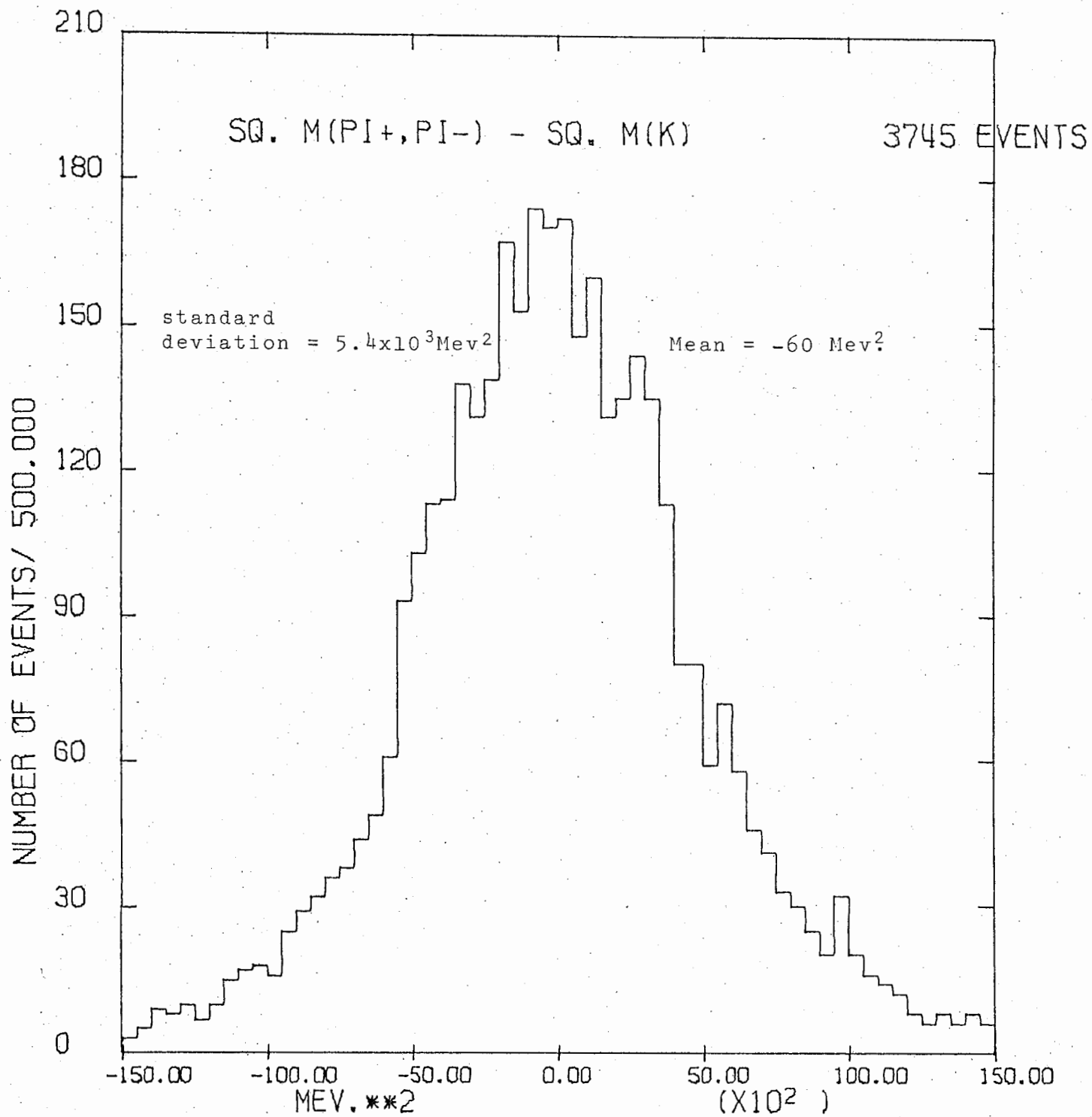
MAGNETIC FIELD

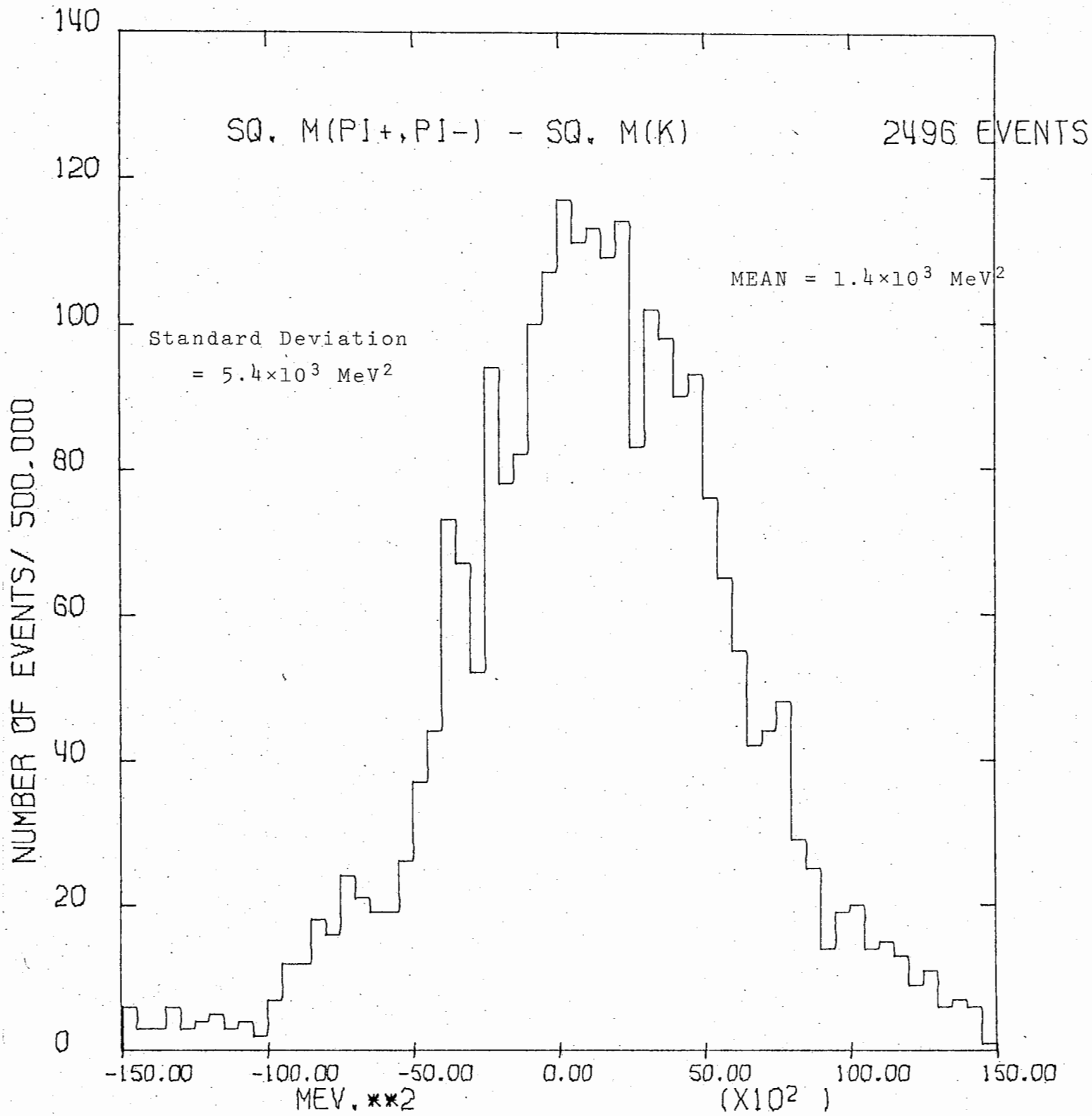
To go from curvature to momentum it is crucial that we know the strength and direction of the magnetic field at every point within the bubble chamber.

The B_x and B_z components of the field were measured at approximately 1200 points using a search coil extended into the bubble chamber. A least squares fit to the data was made using a (25 parameter) set of polynomials satisfying Maxwell's equations. This gives us the field direction and magnitude at every point in space.

A sensitive test of the magnetic field is to use the TVGP (measured) information on the decay tracks of a K^0 to calculate the K^0 mass. We found a decrease in the field of 0.5% was needed to obtain the accepted value of the K^0 mass. Correlations in the reconstructed value of the mass as functions of the tracks' positions in the chamber were examined. A small correlation in the vertical (z) direction was removed by scaling the field by the factor $(Z-21) \times 1.5 \times 10^{-4}$. The following pages show histograms of the invariant mass squared of $\pi^+\pi^-$ from K^0 decays with the accepted value of $M^2(K^0)$ ($248 \times 10^3 \text{ MeV}^2$) subtracted off for both the corrected field and the uncorrected field. The positional dependence of the reconstructed mass showing the correlation and with the correlation removed is also shown.

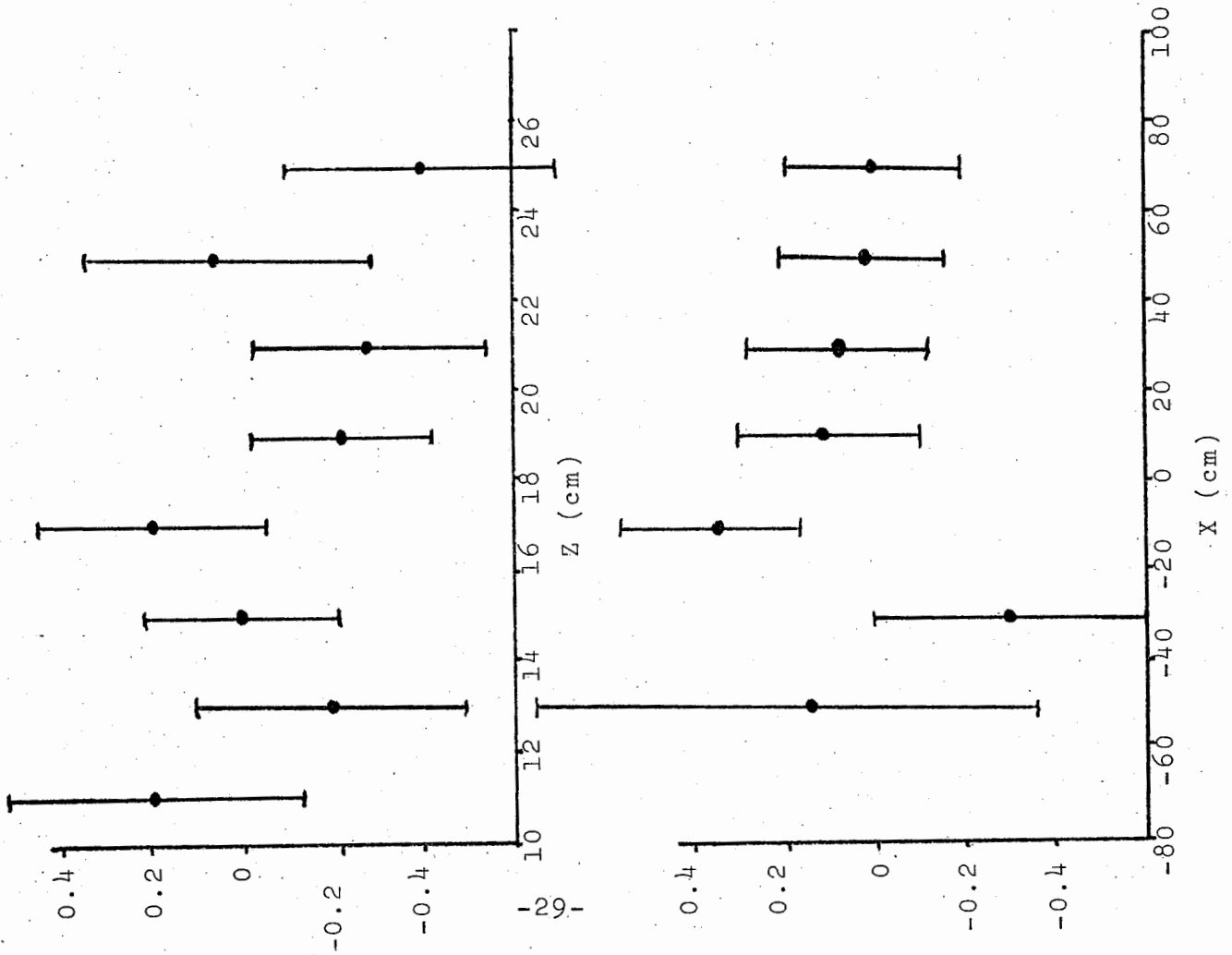
CORRECTIONS TO THE FIELD INCLUDED





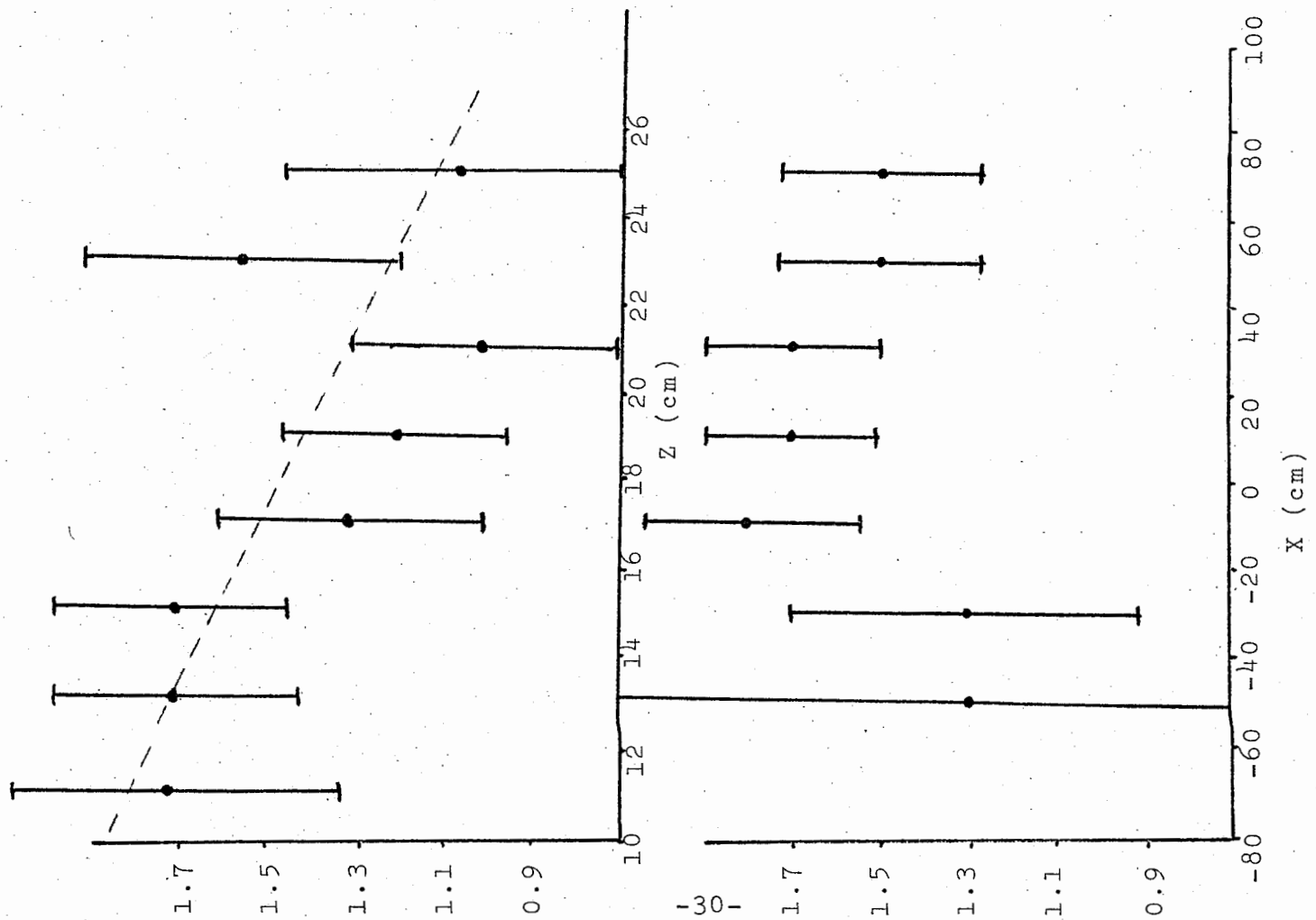
M(K⁰)-497.71 (MeV) with Field Corrections

3813 Events



M(K⁰)-497.71 (MeV) with no Field Corrections

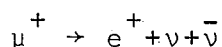
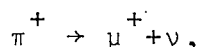
2548 Events



RANGE

If we can determine that a particular track stops in the bubble chamber, then the momentum determined from its range is much more accurate than from curvature. Those tracks which obviously do stop are flagged at the scanning stage and then TVGP calculates the momentum from length.

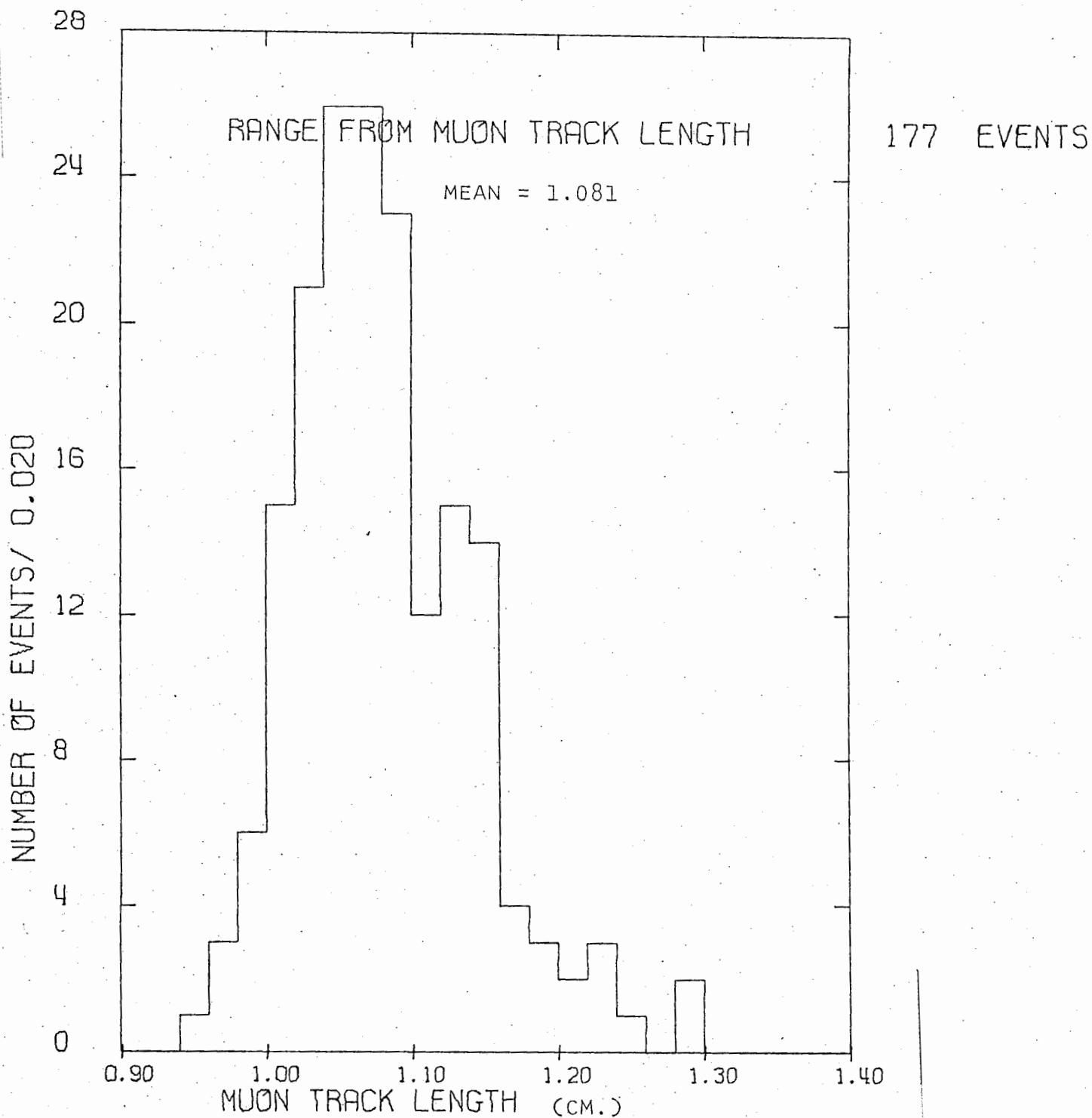
The equation relating range to momentum depends on the operating density of the hydrogen. To calculate this we use the decay chain:



with mean lives of the order of 10^{-8} and 10^{-6} sec. To observe the first decay in the bubble chamber means that the π^+ had to be sufficiently slow not to escape in 10^{-8} sec. But such a slow π^+ will always stop in hydrogen. Therefore π^+ decay occurs at rest in a bubble chamber (π^- is usually captured by a hydrogen nucleus before it can decay). This means that all μ^+ 's from this decay will have the same momentum (29.79 MeV/c) and therefore will stop long before they decay. We measure 262 of these π - μ - e decays and select those events whose muon track satisfies the following criteria

- 1) Error in length less than 0.09 centimeters
- 2) FRMS less than 7 microns.
- 3) Angle the track makes with optical axis is greater than 60 degrees.

The average length of the decaying μ^+ for these events is determined to be 1.081 centimeters. Then we know that μ^+ s' with momentum 29.79 Mev/c travel 1.081 centimeters in the hydrogen before stopping and the density is easily determined.



PULLS

In the fitting procedure we start with measured values for the track parameters (\vec{m}) and finish with fitted values (\vec{x}). Because of the inherent measuring errors the fitted and measured track variables will be different. If we interpret \vec{x} as, in some sense, the "true" variables then in many measurements of the track we will on the average get \vec{x} . Furthermore, if our track parameters have a Gaussian distribution then $(\vec{x}-\vec{m})$ will also have a Gaussian distribution with mean zero. The normalized variables:

$$\Sigma_i \equiv \frac{x_i - m_i}{\sigma_i} = \frac{x_i - m_i}{\sqrt{\sigma_{M_i}^2 - \sigma_{x_i}^2}}$$

are called the pulls and will have (insofar as the assumptions above are valid) a normalized Gaussian distribution (i.e. mean of zero and standard deviation of one). Instead of many measurements of one track we extend the definition of the pull to one measurement of many tracks and examine whether these quantities have a normal Gaussian distribution.

If a pull is not centered on zero, it indicates a systematic bias in the reconstruction of that parameter. A standard deviation greater or less than one means that the assigned errors in that parameter are too small or too large.

To investigate the pulls a sample of (4-C) non-strange events (simple topology events with no vees or kinks) was used. To center the pulls (no zero) we decreased the measured slope of

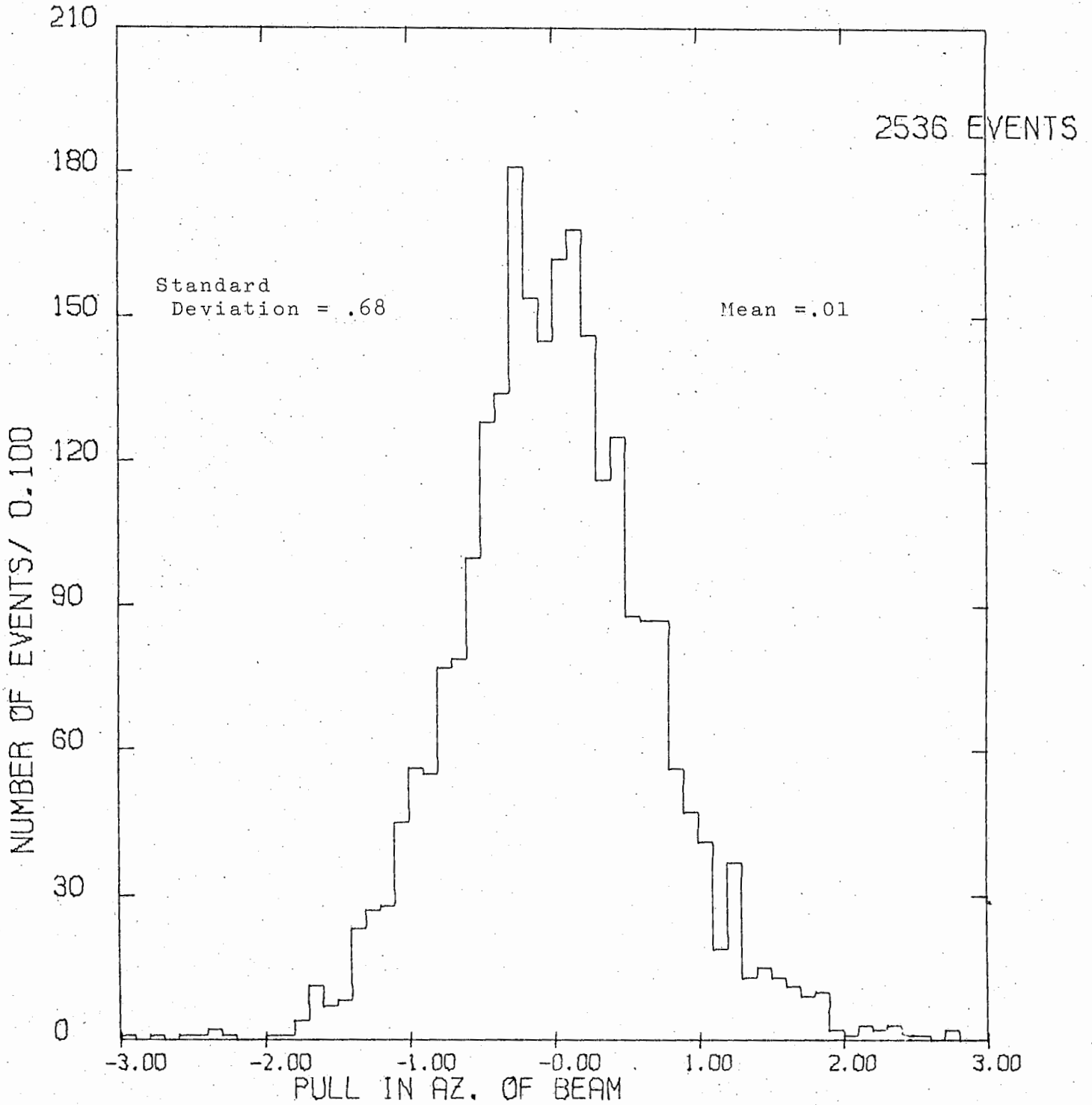
the beam ($\tan\lambda$) by 0.37 standard deviations (a 10% change) and decreased the measured azimuth (ϕ) by 0.05 standard deviations (a change of 0.001%). This shift is probably due to a bias in reconstructing the depth of the points in the chamber. The beam is the most sensitive to this because it travels much further in the bubble chamber than any other track.

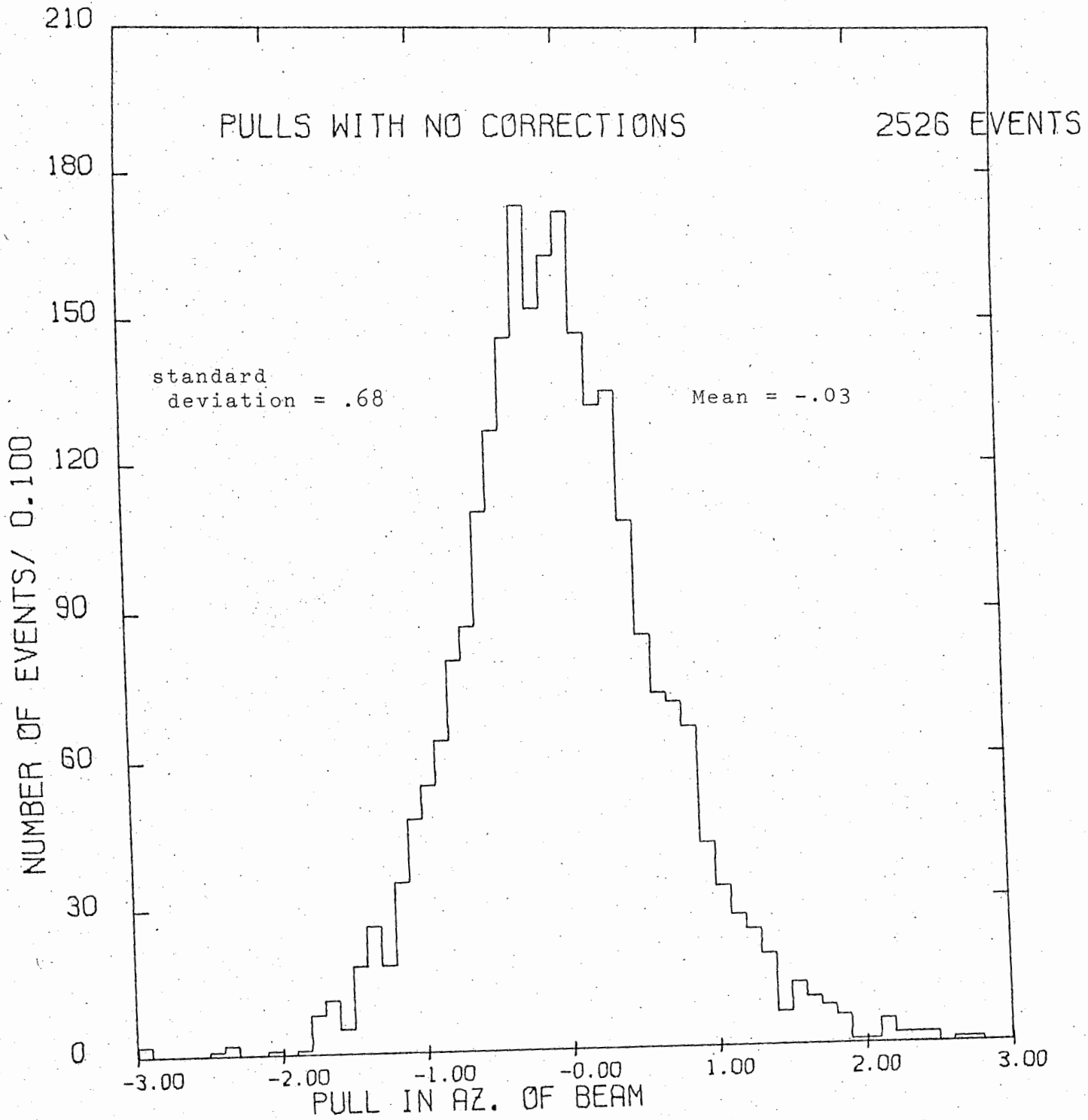
Shifting the beam parameters also benefited the pulls in the outgoing tracks since they are connected by energy-momentum conservation. The following pages present histograms of the pulls in both the beam and the outgoing tracks with the corrections to the beam parameters included and the pulls in the beam parameters with no corrections.

BEAM MOMENTUM

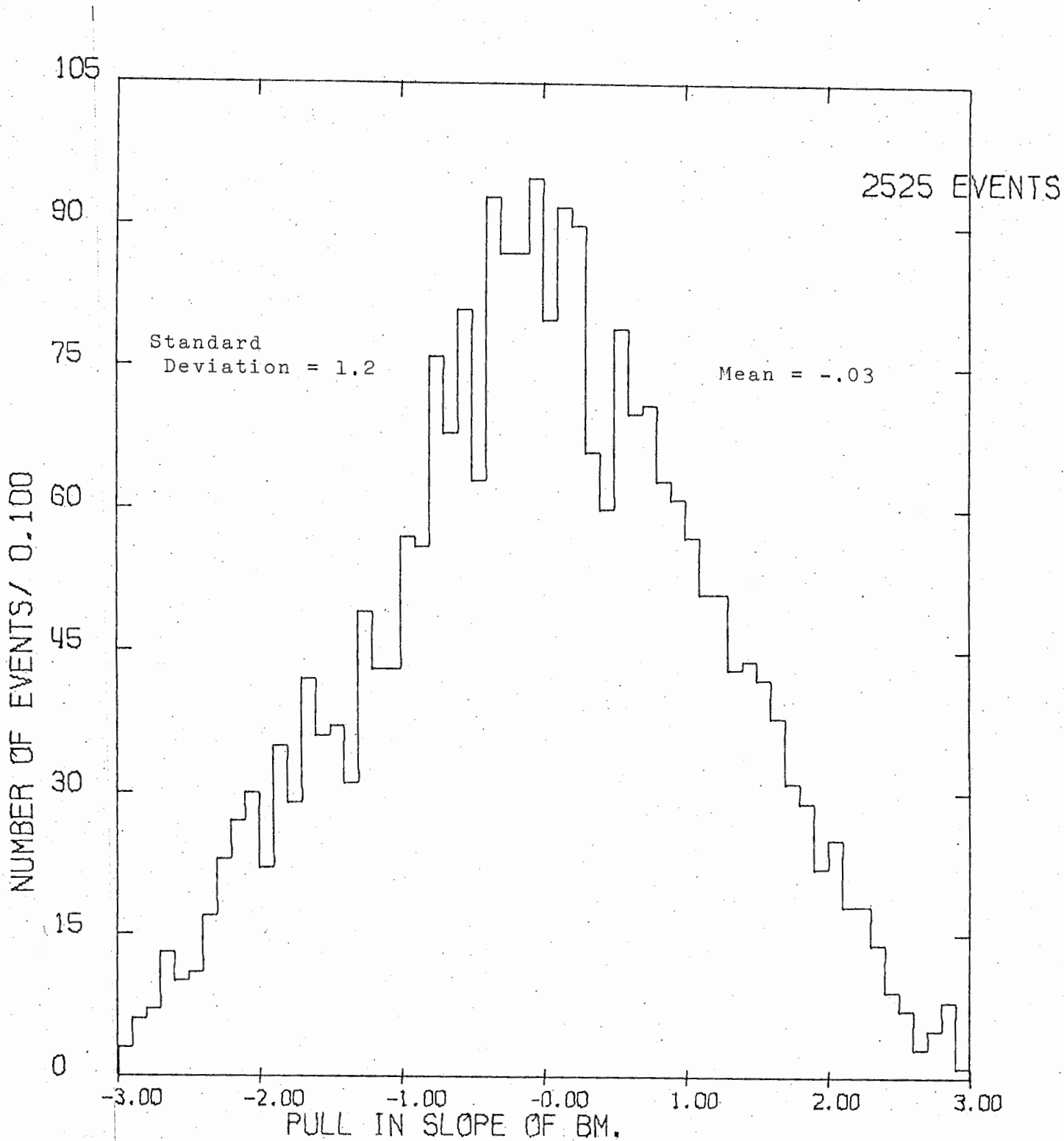
The beam into the bubble chamber has a momentum bite of 5% ($\frac{\Delta p}{p} = 5\%$) in the horizontal (y) direction. To exhibit this momentum spectrum the beam is dispersed in the y-direction just before it enters the chamber. This leads to a correlation between the beam momentum and entrance position of 5 cm. per percent $\frac{\Delta p}{p}$ (i.e. a beam spread of 25 cm). This means that given the entrance point at the window of any beam track we should be able to calculate its momentum. This is particularly useful in the case of events where the beam travels a short distance before interacting, for then the error on the measured value of the momentum is quite large

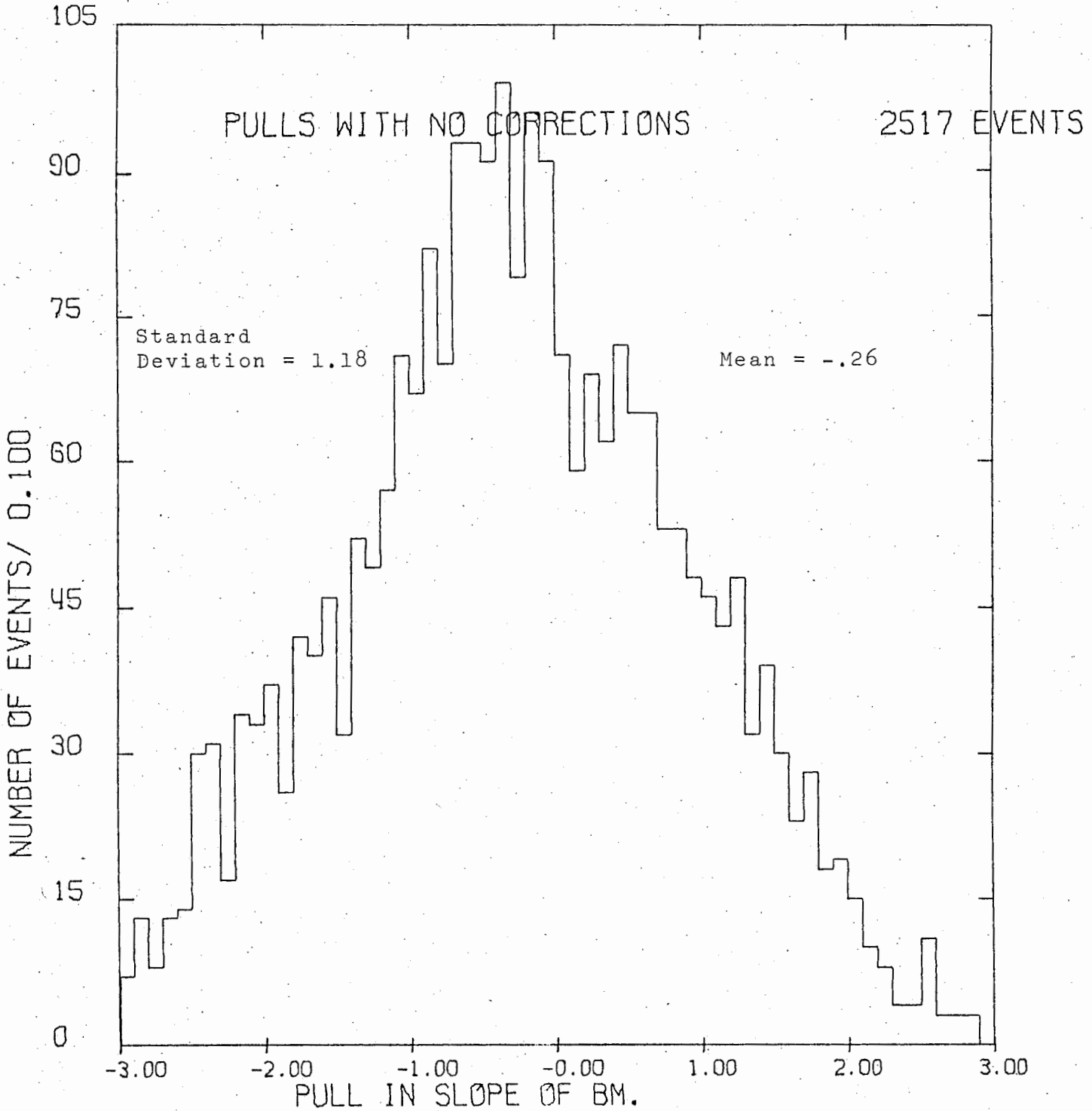
Corrected Pull



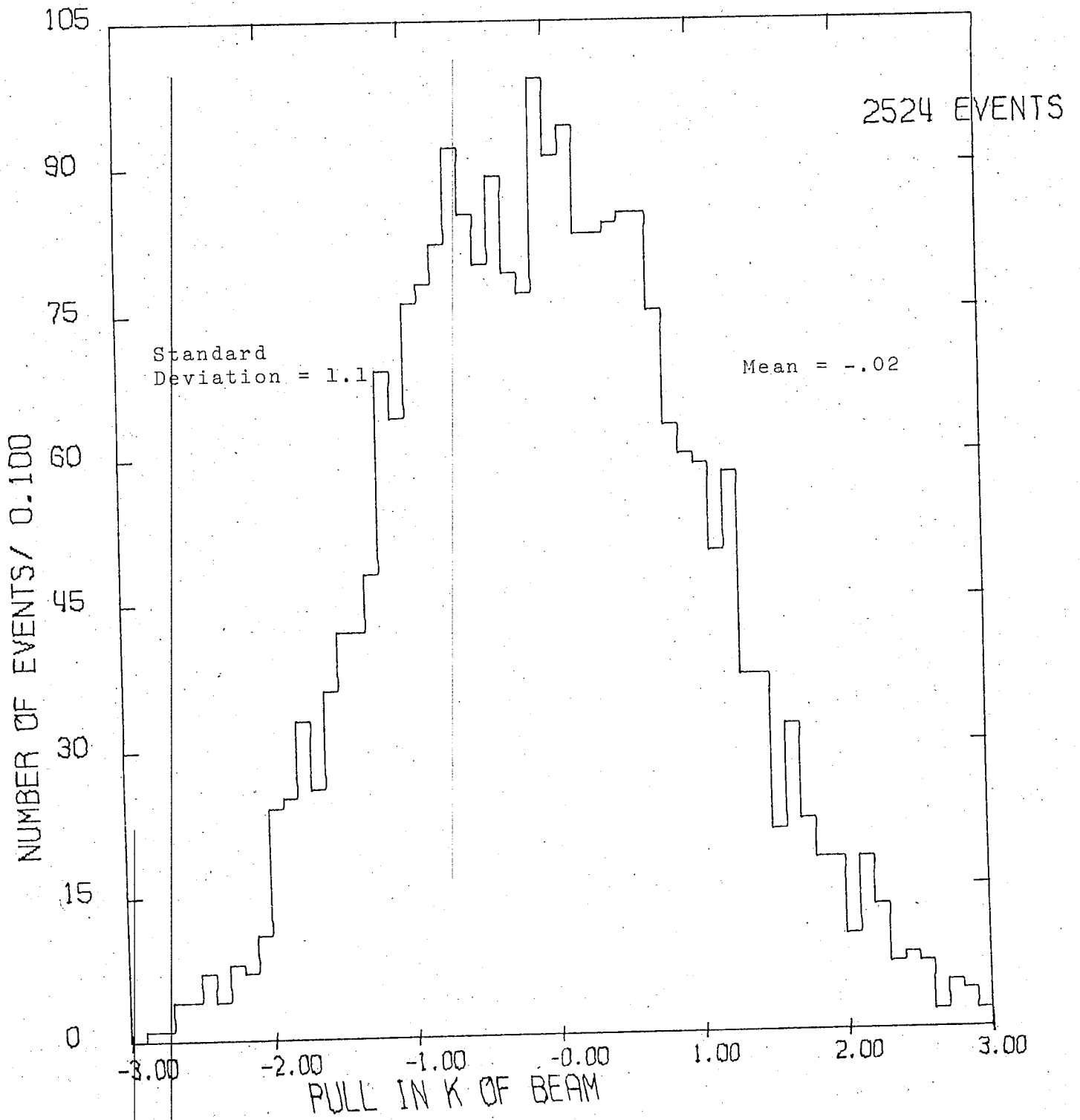


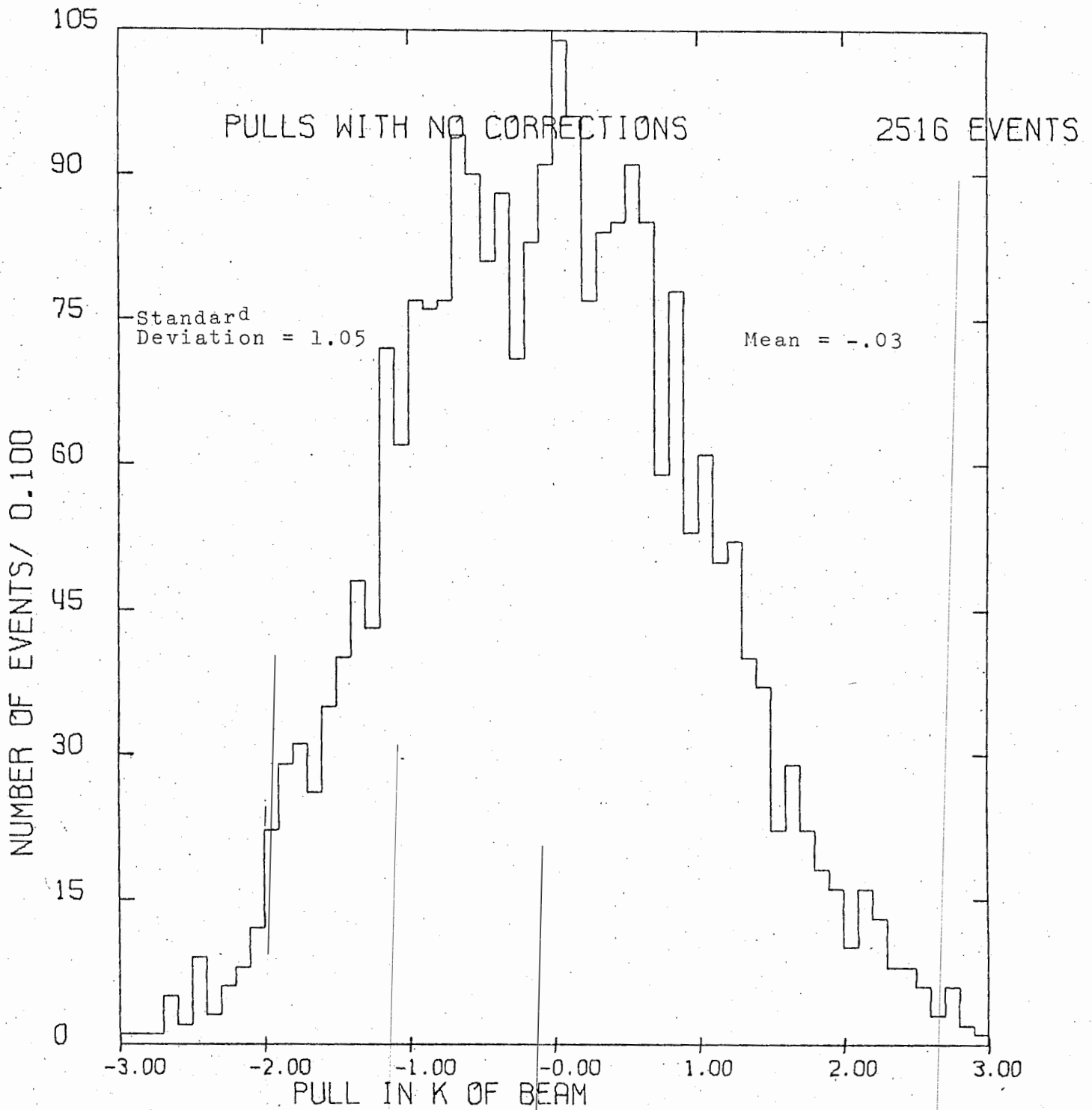
Corrected Pull



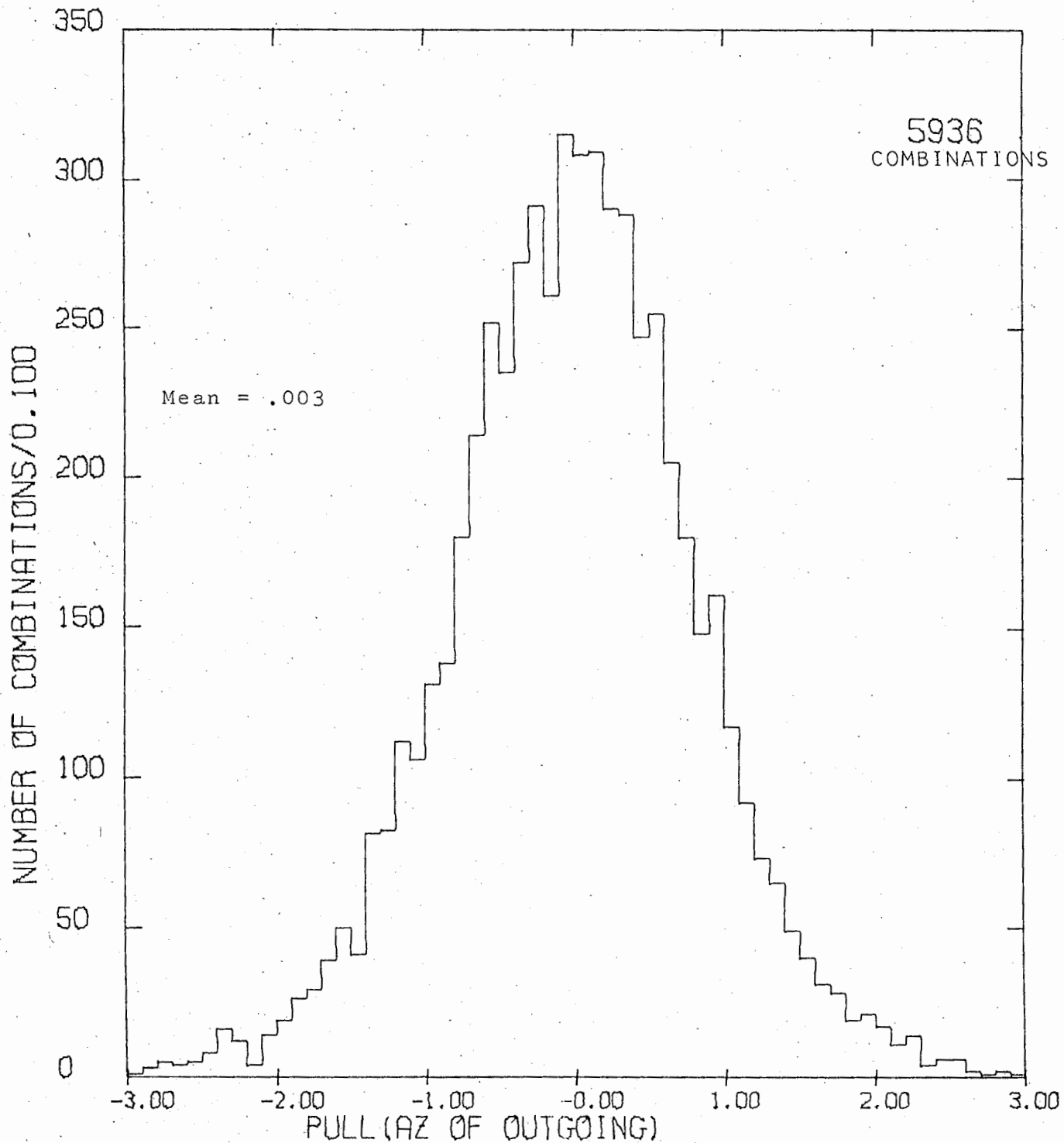


Corrected Pull

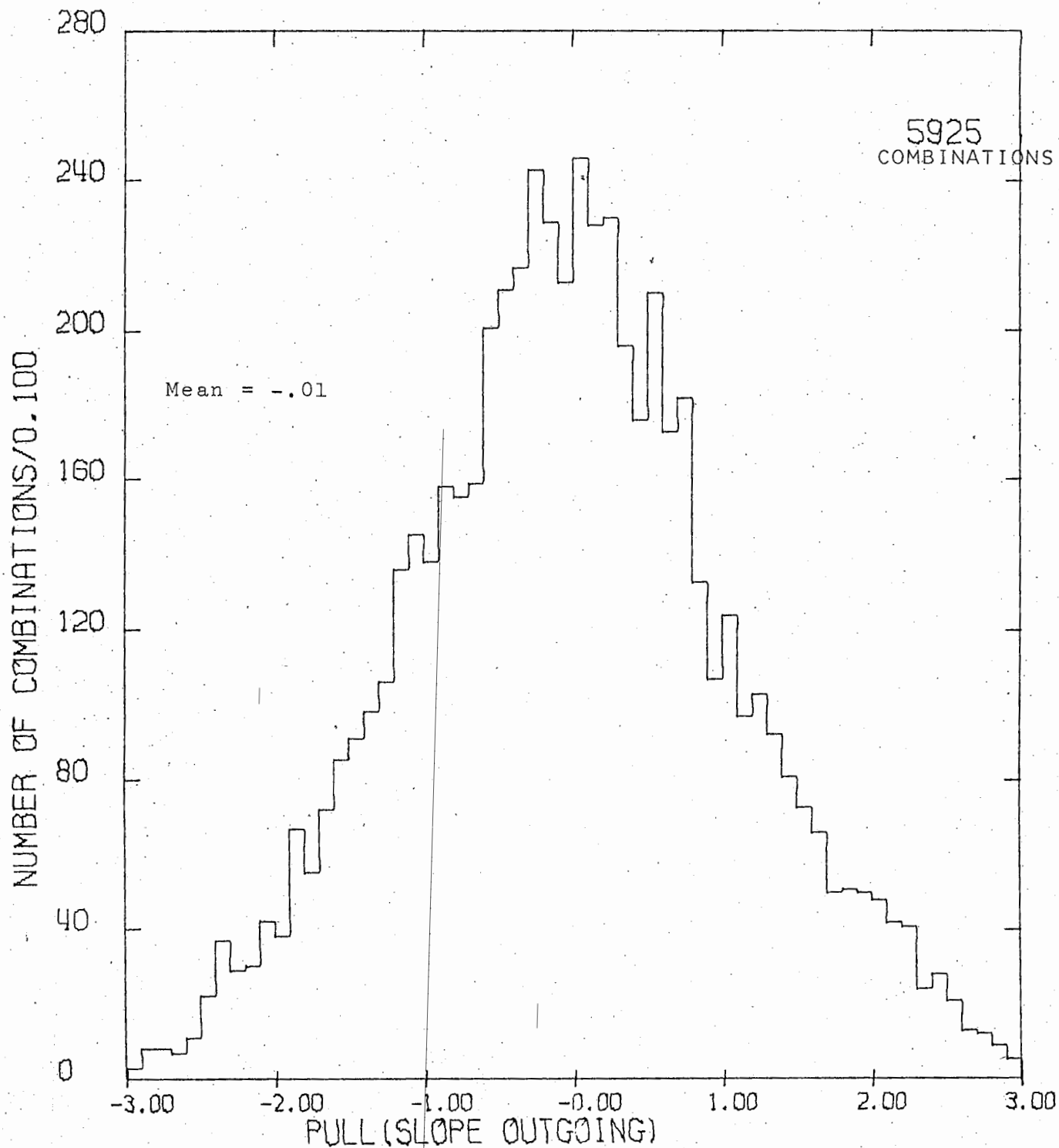




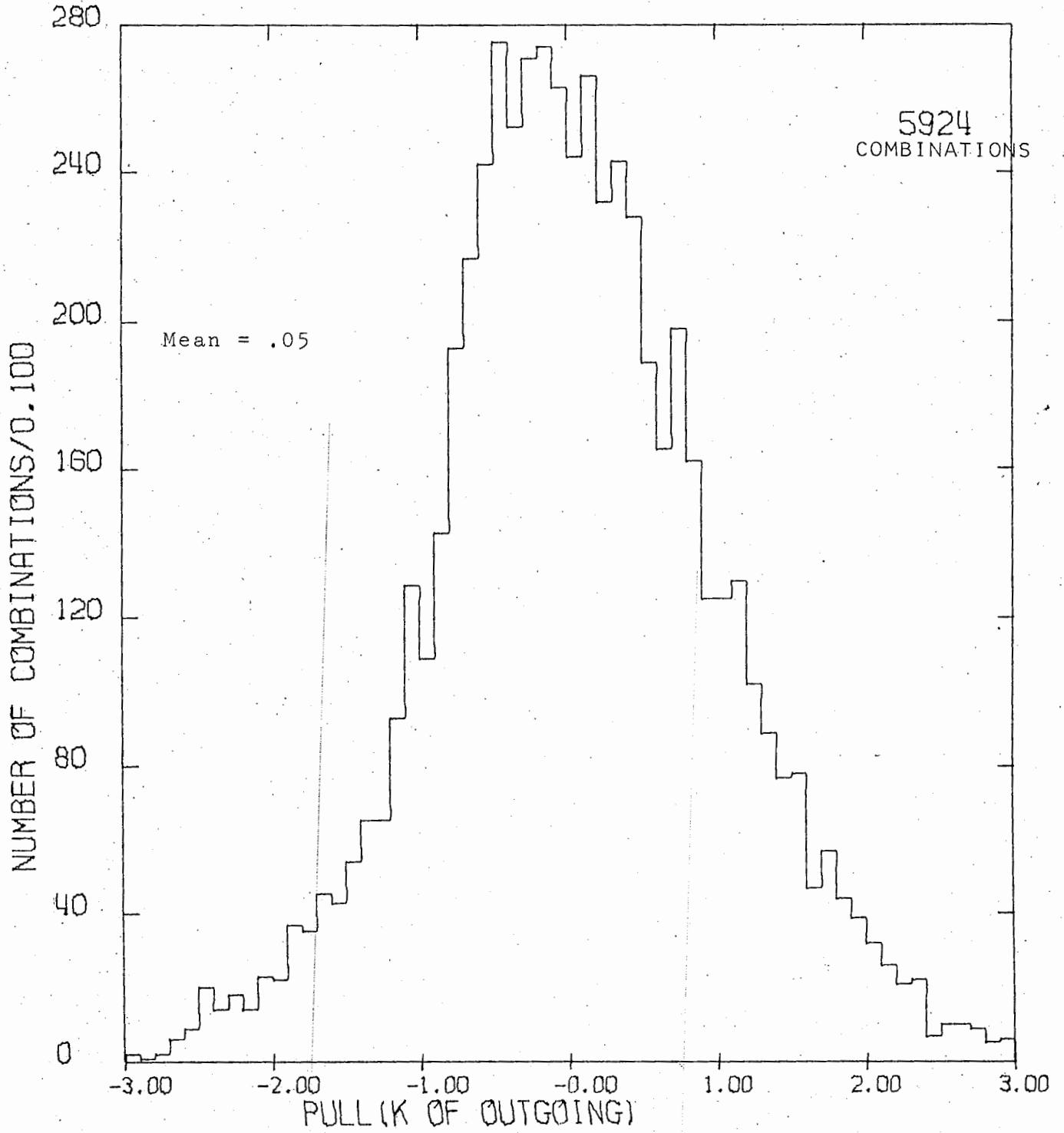
Corrected Pulls



Corrected Pulls



Corrected Pulls



($\approx 10\%$), whereas our calculated value is very precise.

Every interaction that takes place in the bubble chamber can be located by the co-ordinates of the entrance point at the window (y_w, z_w) and the length of beam before interaction (x). Using a sample of non-strange (4-C) fits the co-ordinates of the vertex were "swum" back (using a rough value for the beam curvature) to find the point at which the beam track passed through the window. By suppressing the measured momentum of the beam we turned these events into 3-C fits and obtained a fitted value for the beam momentum (p_f) for each event. We parameterized p_f in the form: $p_f = p_o + Ax + By_w + Cz_w$ and did a least squares fit to the parameters p_o, A, B, C . The fitted values obtained were: 10215 MeV, -0.4 MeV/cm, 20.1 MeV/cm, -1.7 MeV/cm. This gave us a very accurate prediction of the beam momentum for any interaction.

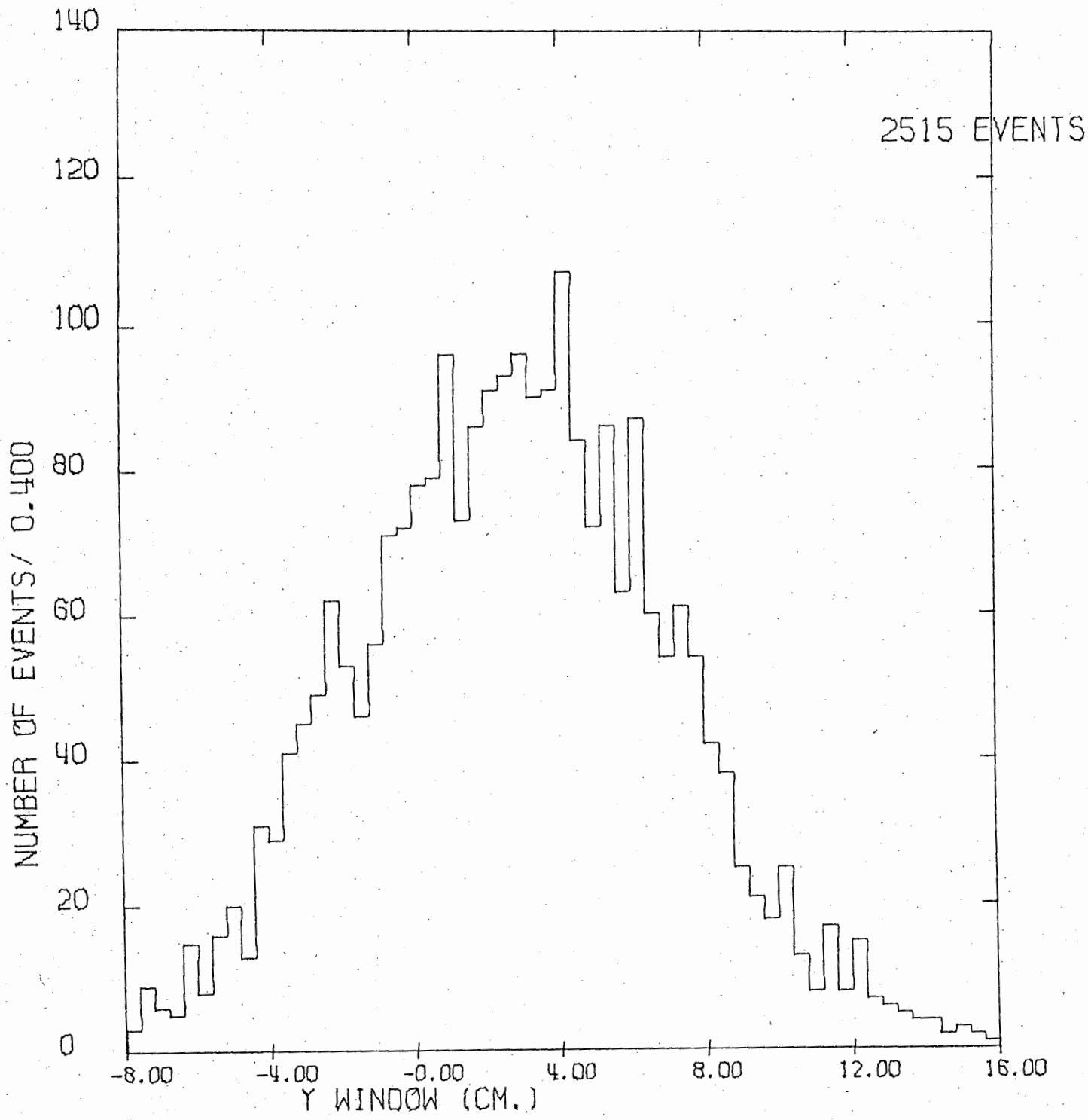
The last part of the beam line focuses the collimator F2 onto the bubble chamber (see page 8). The momentum resolution is limited by the (non-point like) image of F2. In this case the image has a horizontal spread of 18 mm which corresponds to a spread in momentum of 21 MeV/c. This is the accuracy of our predicted value.

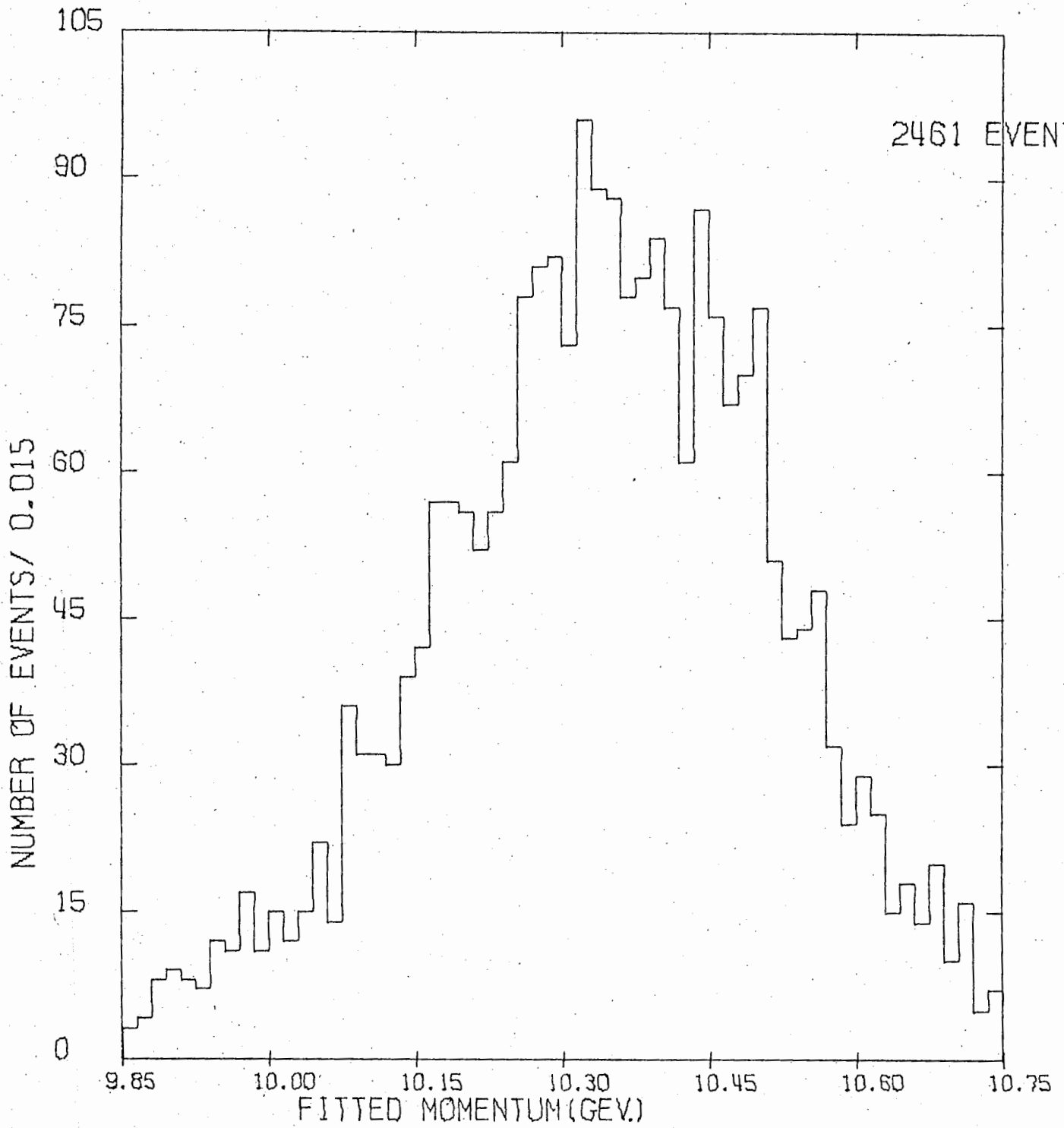
We form a new value for the beam momentum (called the BMAVG value) by taking a weighted average of the predicted and measured values (in practice the predicted value completely dominates because of its small error). This replaces the

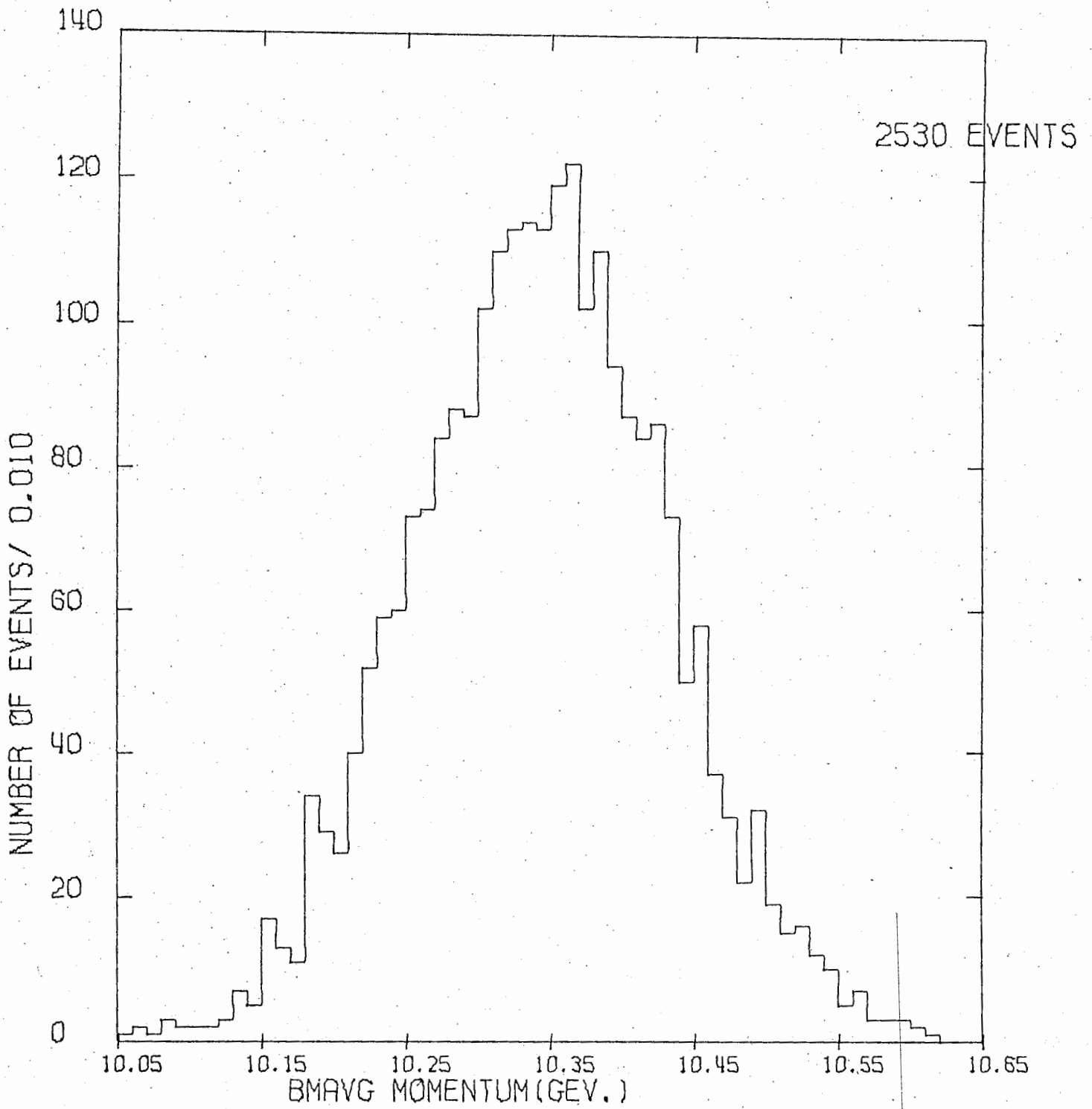
measured value and becomes the new first approximation in the fitting procedure.

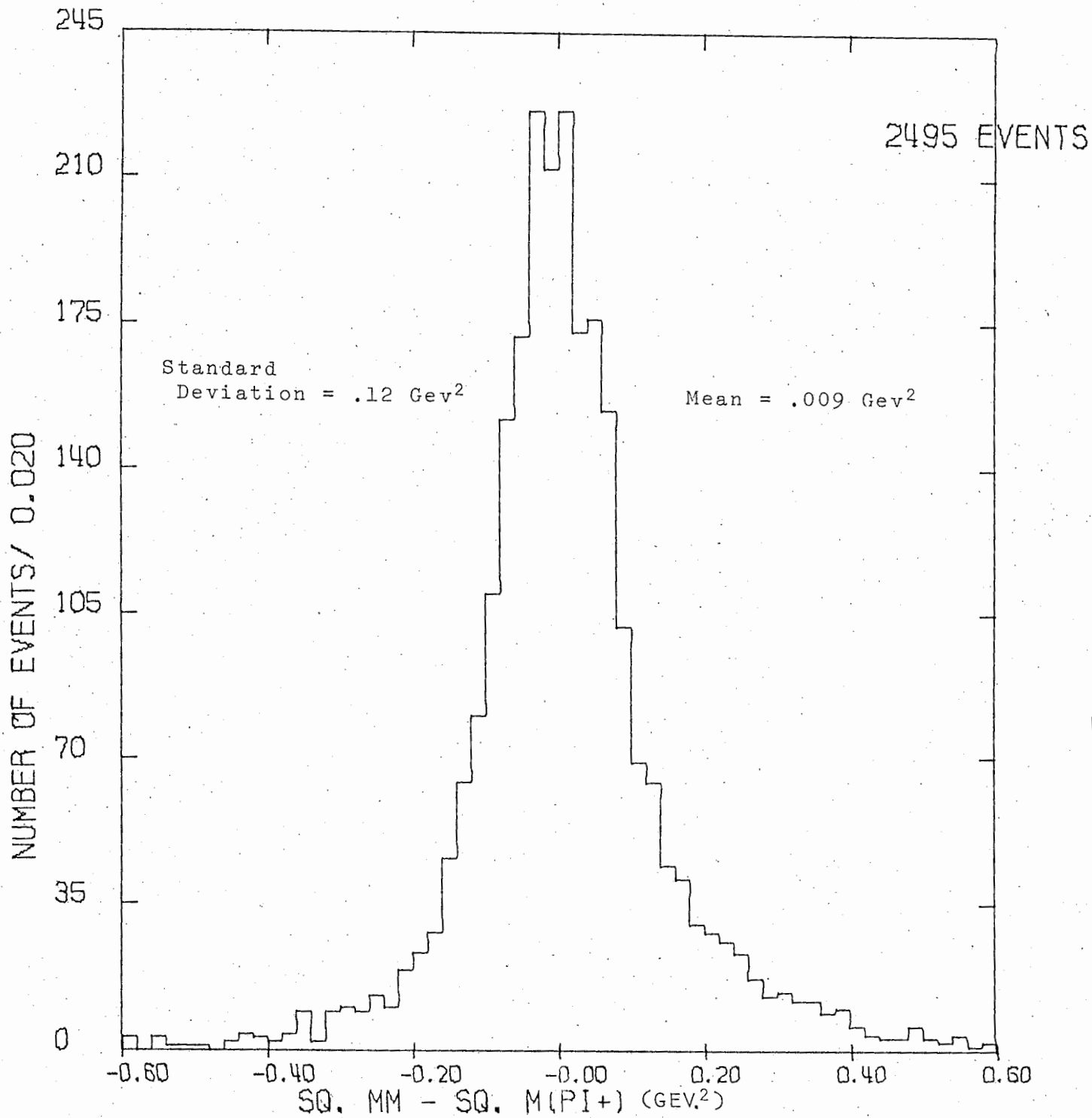
MISSING MASS

Since the incoming particle (π^+) is a constant for all events it is a useful consistency check to try to reproduce this mass using our measured parameters. Using non-strange events which had a good 4-C fit we adopted the mass assignments from the fit and used four-momentum conservation and the measured parameters for all tracks to calculate the incoming mass for each event. On page 50 is a histogram of the square of this calculated mass (the missing mass) with the square of the π^+ mass subtracted off. The mean is 0.009 GeV².









$\pi^+ p \rightarrow K^{*+}(890) \Sigma^+(1385)$

PHYSICS ANALYSIS

We have extracted from the experiment those events producing (visible) strange particles and the four-momentum of all particles taking part in the interaction has been determined by fitting the reaction to the allowed final states. Systematic errors in the measured track parameters have been removed so that the final fitted parameters are free of bias. The following page indicates the number of events in the most common final states, both unique fits and total fits (i.e. ambiguous fits included). These numbers are from combined Toronto and Brookhaven data but are only preliminary since they include only about 70 percent of the Toronto data.

This puts us in the position of being able to analyse the physics that underlies the production processes. As an example of this analysis we present an examination of the quasi two-body reaction $\pi^+ p \rightarrow K^{*+}(890) \Sigma^+(1385)$.

$$\underline{\pi^+ p \rightarrow K^{*+}(890) \Sigma^+(1385)}$$

The final state $K^{*+}(890) \Sigma^+(1385)$ is present in the following two channels:

Channel A: $(\Lambda \pi_S^+) (K^0 \pi_f^+)$ $\pi_{s,f}$ = slow, fast pion

(Because of the peripheral nature of the production the fast π^+ almost always comes from $K^{*+}(890)$ rather than $\Sigma^+(1385)$).

Channel B: $(\Lambda \pi^+) (K^+ \pi^0)$

Final State	Total Fits	Unique Fits
$nK^+\bar{K}^0\pi^+$	783	92
$nK^0\bar{K}^0\pi^+\pi^+$	77	45
$nK^+\bar{K}^0\pi^+\pi^+\pi^-$	855	99
$nK^-\bar{K}^0\pi^+\pi^+\pi^+$	205	35
$nK^0\bar{K}^0\pi^+\pi^+\pi^+\pi^-$	32	5
$pK^+\bar{K}^0$	187	181
$pK^+\bar{K}^0\pi^0$	860	303
$pK^0\bar{K}^0\pi^+$	1255	643
$pK^0\bar{K}^0\pi^+\pi^0$	183	130
$pK^+\bar{K}^0\pi^+\pi^-$	529	269
$pK^+\bar{K}^0\pi^+\pi^-\pi^0$	1560	285
$pK^0\bar{K}^0\pi^+\pi^+\pi^-$	1100	122
$pK^-\bar{K}^0\pi^+\pi^+$	329	180
$p^-\bar{K}^0\pi^+\pi^+\pi^0$	663	130
$pK^0\bar{K}^0\pi^+\pi^+\pi^-\pi^0$	83	53

Continued on next page.....

Final State	Total Fits	Unique Fits
$\Lambda K^+ \pi^+$	354	304
$\Lambda K^0 \pi^+ \pi^+$	1455	361
$\Lambda K^+ \pi^+ \pi^0$	1564	522
$\Lambda K^0 \pi^+ \pi^+ \pi^0$	261	209
$\Lambda K^+ \pi^+ \pi^+ \pi^-$	488	236
$\Lambda K^0 \pi^+ \pi^+ \pi^+ \pi^-$	1230	248
$\Lambda K^+ \pi^+ \pi^+ \pi^- \pi^0$	2078	634
$\Lambda K^0 \pi^+ \pi^+ \pi^+ \pi^- \pi^0$	162	93
$\Sigma^+ K^0 \pi^+$	59	55
$\Sigma^+ K^0 \pi^+ \pi^0$	187	56
$\Sigma^+ K^0 \pi^+ \pi^+ \pi^-$	66	58
$\Sigma^+ K^0 \pi^+ \pi^+ \pi^- \pi^0$	135	32
$\Sigma^- K^0 \pi^+ \pi^+ \pi^+$	24	23
$\Sigma^- K^0 \pi^+ \pi^+ \pi^+ \pi^0$	41	9
$\Sigma^0 K^+ \pi^+$	92	20
$\Sigma^0 K^0 \pi^+ \pi^+$	265	25
$\Sigma^0 K^+ \pi^+ \pi^+ \pi^-$	164	24
$\Sigma^0 K^0 \pi^+ \pi^+ \pi^+ \pi^-$	151	10

On the following pages are histograms of the $(K, \pi)^+$ invariant mass and the $(\Lambda, \pi)^+$ invariant mass for the two channels combined. We see the large $(K, \pi)^+$ resonance at approximately 890 Mev. which we call the $K^{*+}(890)$ resonance (the $K^{*+}(1420)$ is also clearly visible). On the other histogram we identify the $(\Lambda, \pi)^+$ resonance at 1385 Mev. which is the $\Sigma^+(1385)$.

To obtain a sample of $K^{*+}(890) \Sigma^+(1385)$ events from these two channels we selected those events for which both invariant masses were in the resonance signal. Specifically we chose those events for which

$$\text{Channel A: } 1.34 \text{ Gev.} < M(\Lambda, \pi_S^+) < 1.46 \text{ Gev.}$$

and

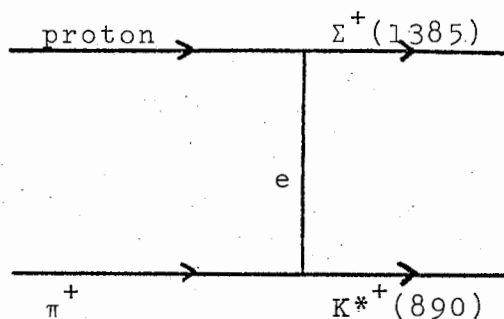
$$0.84 \text{ Gev.} < M(K^0, \pi_F^+) < 1.05 \text{ Gev.}$$

$$\text{Channel B: } 1.30 \text{ Gev.} < M(\Lambda, \pi^+) < 1.46 \text{ Gev.}$$

and

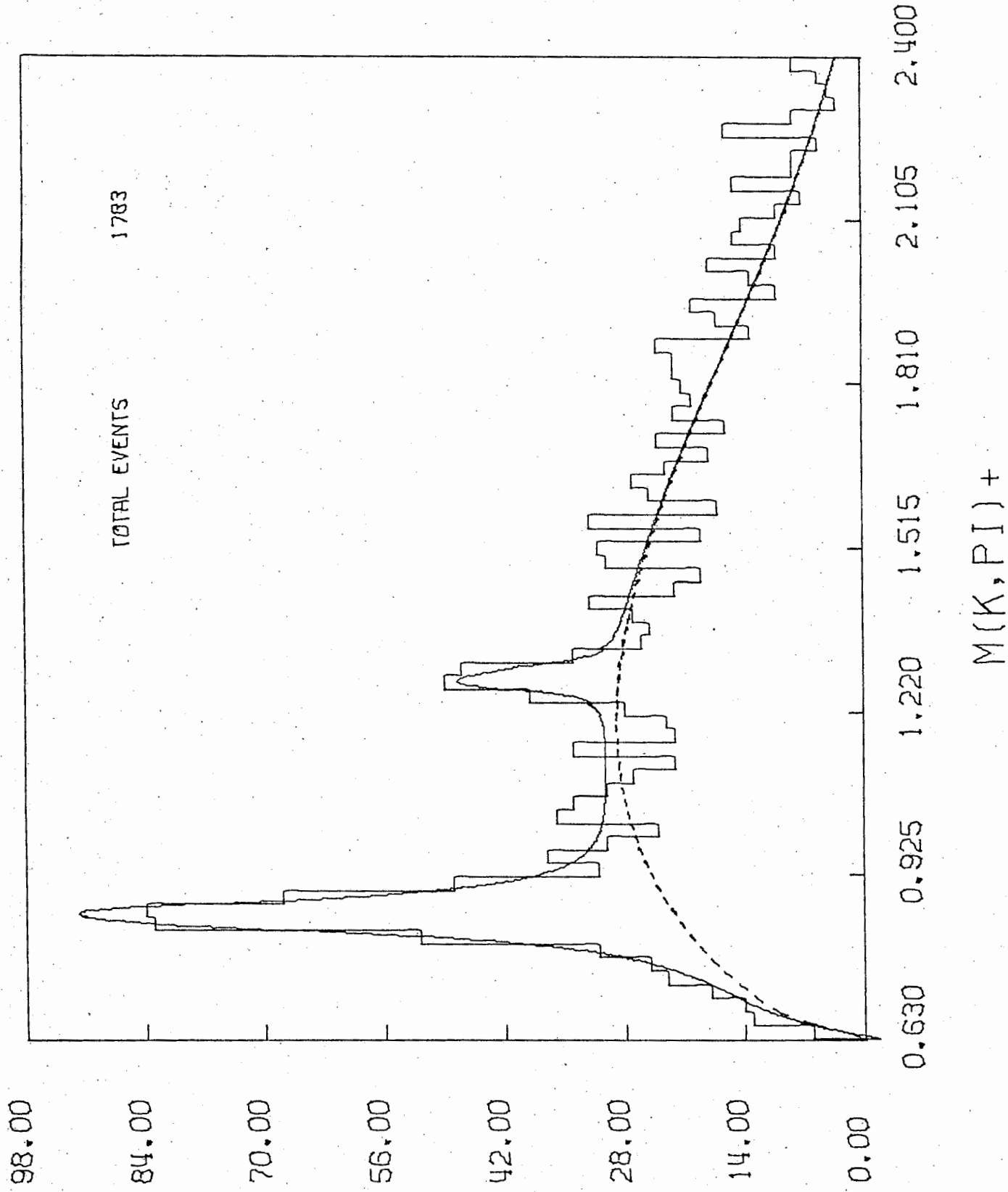
$$0.82 \text{ Gev.} < M(K^+, \pi^0) < 1.00 \text{ Gev.}$$

We can further purify the sample by assuming the process occurs peripherally according to a diagram of the form

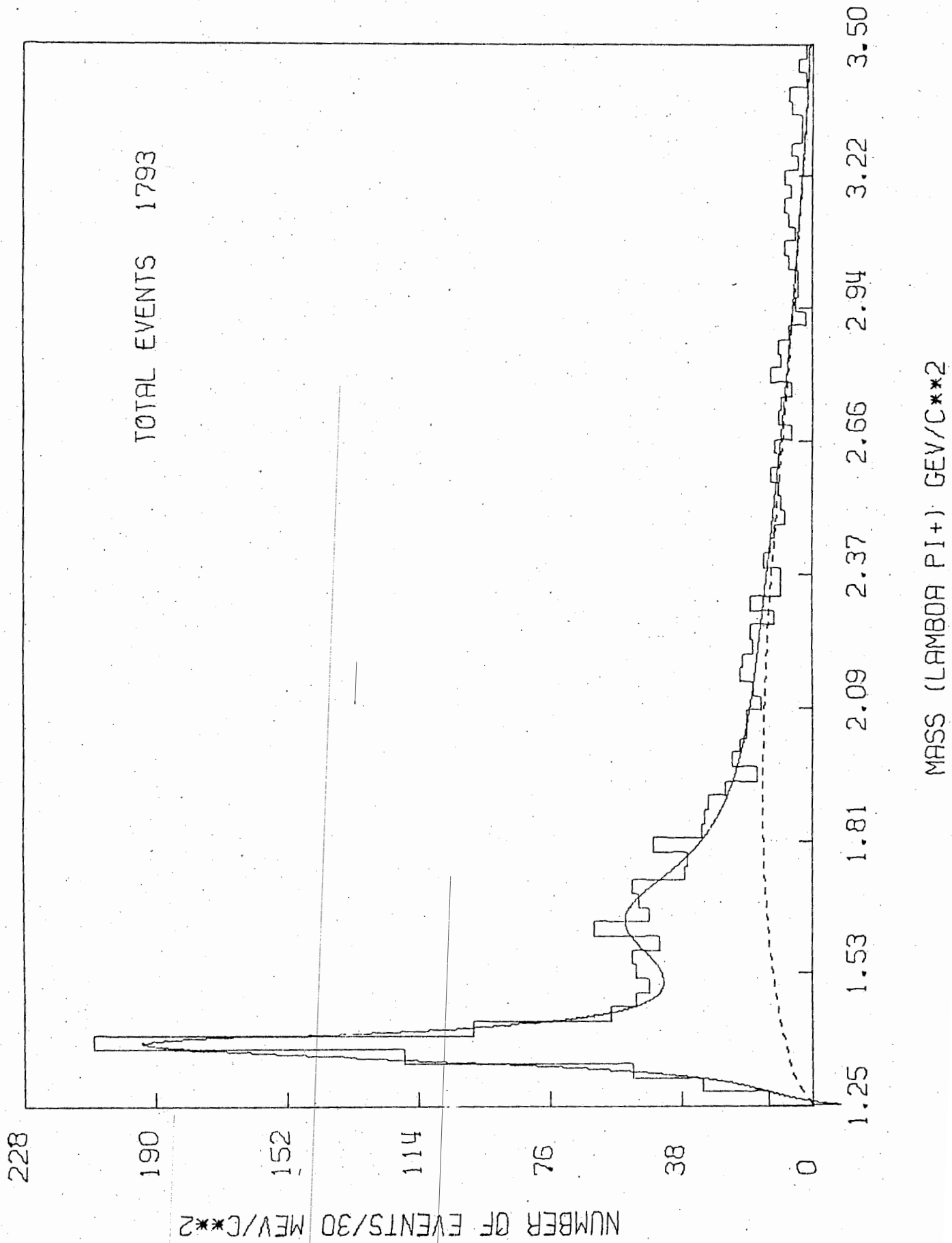


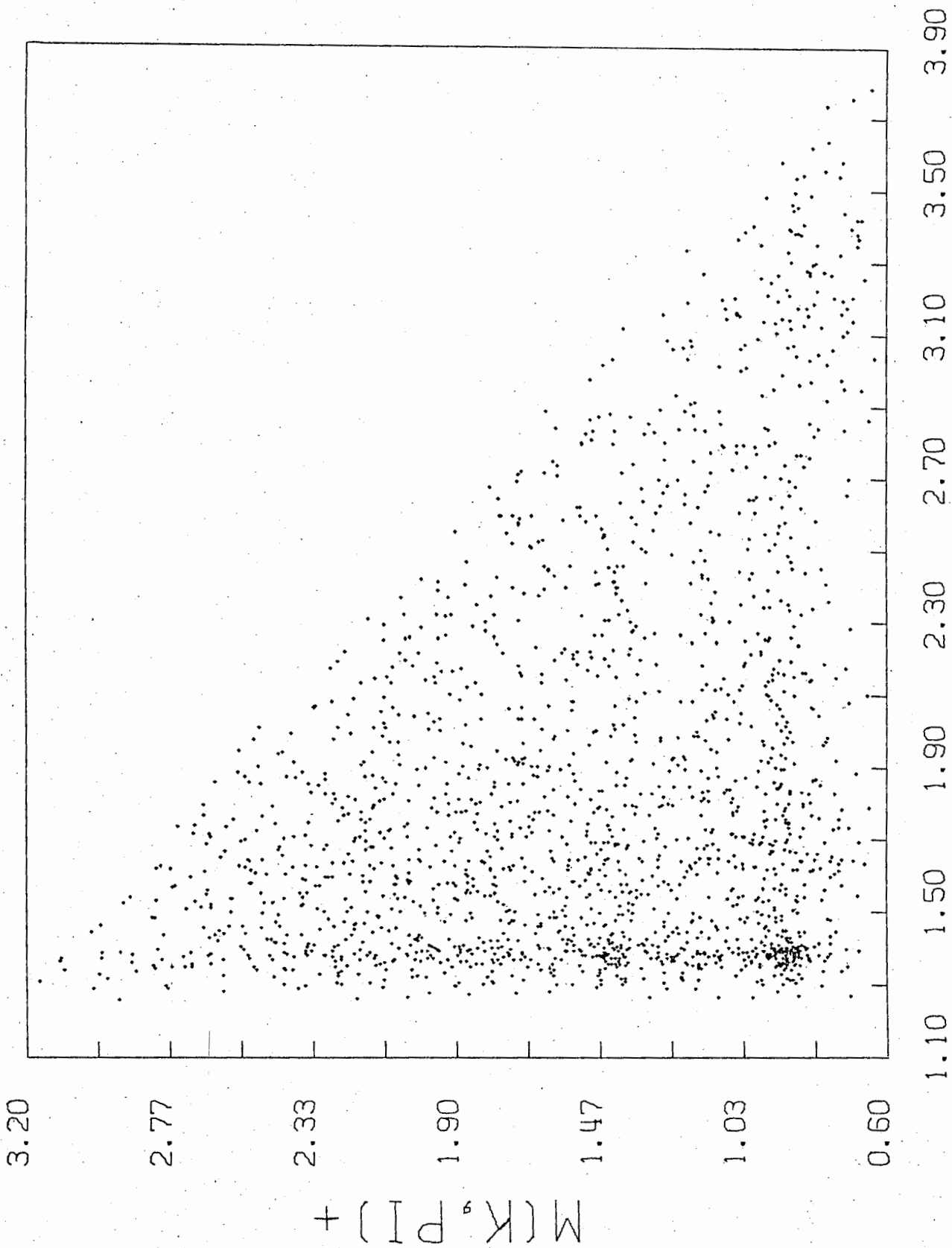
where "e" is a (virtual) exchanged particle. The assumption

$M(K, \pi)^+$ for Channels A and B combined



$M(\Lambda, \pi^+)$ for Channels A and B Combined





MRI OMBDO PT

of peripherality means that the momentum transfer $t \equiv -(p_\pi - p_p)^2$ is small. It is more correct to use $t' \equiv t - t_{\min}$ where t_{\min} is the minimum (kinematically) allowed value of t for that event. Because of the finite width of a resonance t_{\min} will vary across the resonance (see page 58) and this makes t' a more correct variable to use. With the limitation to $t' < 1.0$ GeV². We have the following number of events in each channel.

Channel A: 84

Channel B: 41

Note that from isospin coupling we expect Channel A to contain twice as many events as Channel B.

The differential cross section is pictured on page 60. We fit this to a curve of the form $\exp(-\lambda t')$ with $\lambda = 3.2 \pm 0.3$ GeV⁻².

SPIN DENSITY MATRIX

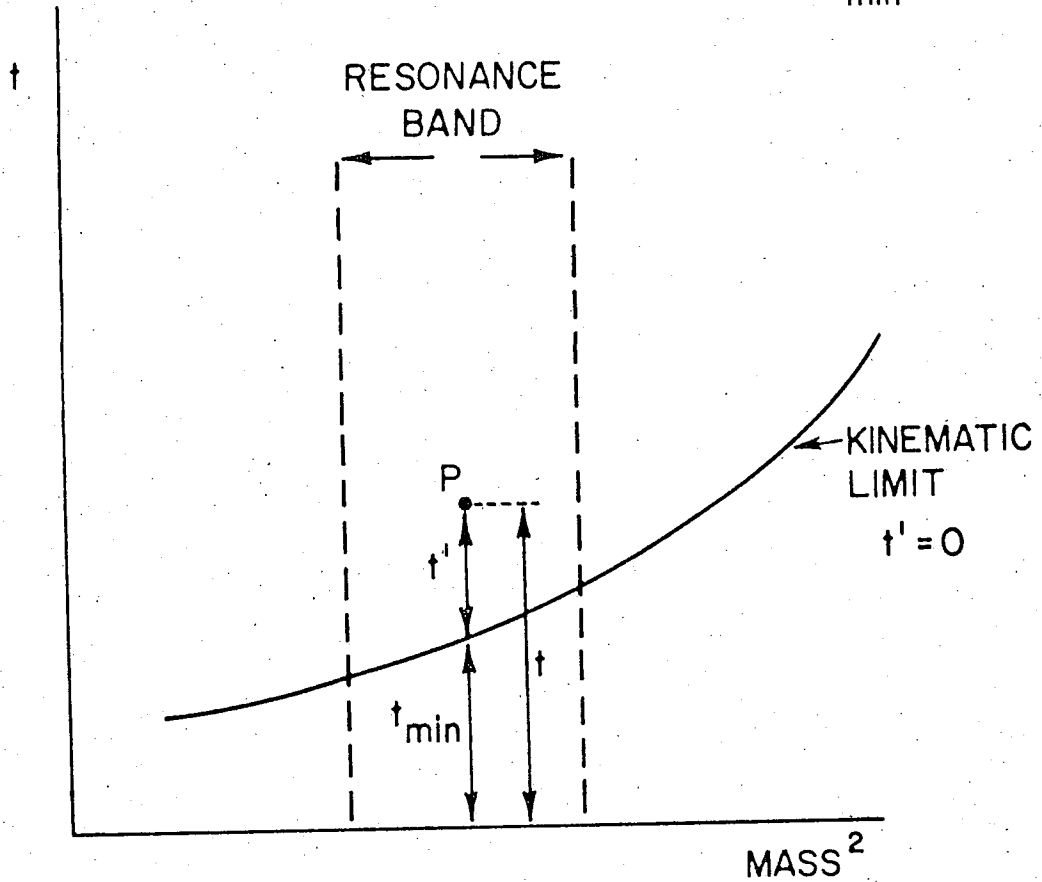
We choose to study this reaction in the Gottfried-Jackson frame (see page 58) where the resonance (either $K^{*+}(890)$ or $\Sigma^+(1385)$) is at rest, with z-axis along the direction of the exchanged particle and the y-axis is the production normal Gottfried (1964). The orientation of the decay particles from the resonance is specified by the polar angles θ, ϕ .

Information on the production mechanism $a+b \rightarrow c+d$ is contained in the spin density matrix which we define as

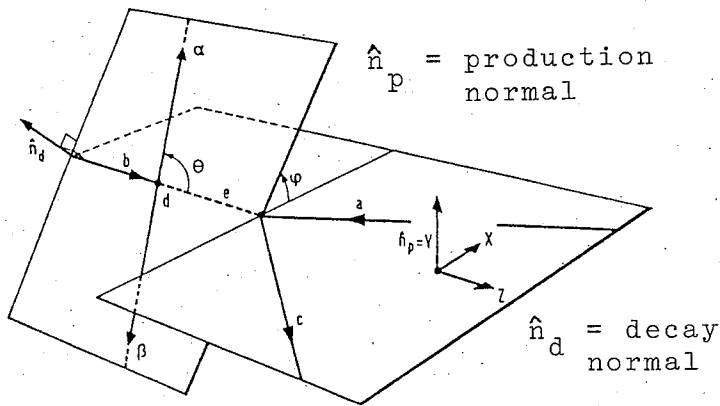
$$\rho_{mm'}^{nn'} \equiv \sum_{K,\ell} \langle m,n | T | K,\ell \rangle \langle m',n' | T | K,\ell \rangle^*$$

where K, ℓ, n, m are J_z values for initial particles and the

$$t' = |t - t_{\min}|$$



CHEW-LOW PLOT



from Khoury
(1972)

Gottfried-Jackson frame for the study of the decay
of a resonance d produced in an interaction
 $a+b \rightarrow c+d$. from Toet (1974)

produced particles. We can particularize to one of the produced particles of spin J ($K^{*+}(890)$ or $\Sigma^+(1385)$) by summing over the other:

$$\rho_{mm'}^J = \sum_n \rho_{mm'}^{nn} = \langle m | 4_J \rangle \langle 4_J | m' \rangle$$

i.e.

$\rho_{mm'}^J$ is a measure of the spin substate populations.

Relations between matrix elements reduces the number of independent parameters (Schmitz (1965)). Our matrix elements become

$$\rho^{K^*} = \begin{pmatrix} \frac{1}{2}(1-\rho_{00}) & \rho_{10} & \rho_{1-1} \\ \rho^{*10} & \rho_{00} & -\rho^{*10} \\ \rho_{1-1} & -\rho_{10} & \frac{1}{2}(1-\rho_{00}) \end{pmatrix} \quad \begin{array}{l} \rho_{00}, \rho_{1-1} \text{ are} \\ \text{real; therefore} \\ 4 \text{ parameters} \end{array}$$

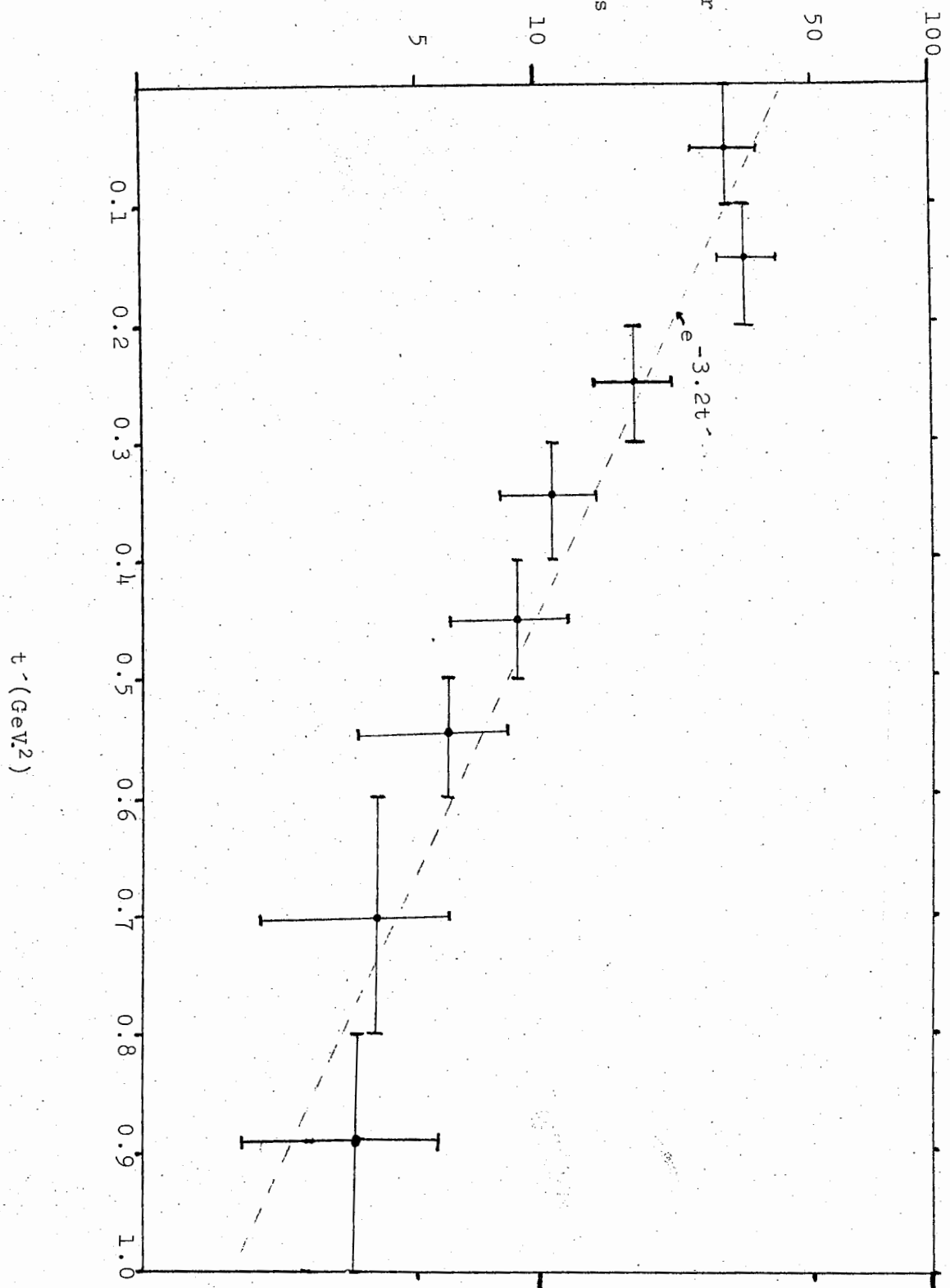
$$\rho^\Sigma = \begin{pmatrix} \rho_{33} & \rho_{31} & \rho_{3-1} & \rho_{3-3} \\ \rho^{*31} & \frac{1}{2}-\rho_{33} & \rho_{1-1} & \rho^{*3-1} \\ \rho^{*3-1} & -\rho_{1-1} & \frac{1}{2}-\rho_{33} & -\rho^{*31} \\ -\rho_{3-3} & \rho_{3-1} & -\rho_{31} & \rho_{33} \end{pmatrix} \quad \begin{array}{l} \text{(written in the} \\ \text{form } \rho_{2m,2m'}) \\ \rho_{33}, \rho_{3-3}, \rho_{1-1} \\ \text{are real} \\ \text{therefore 7 para-} \\ \text{meters} \end{array}$$

The angular distributions for resonance decay $W(\theta, \phi)$ can be calculated in terms of the density matrix elements.

$$W_{K^*}(\theta, \phi) = \frac{3}{4\pi} \left[\frac{1}{2}(1-\rho_{00}) + \frac{1}{2}(3\rho_{00}-1)\cos^2\theta - \rho_{1-1}\sin^2\theta\cos 2\phi - \sqrt{2}\text{Re}\rho_{10}\sin 2\theta\cos\phi \right]$$

$$W_\Sigma(\theta, \phi) = \frac{3}{4\pi} \left[\frac{1}{6}(1+4\rho_{33}) + \frac{1}{2}(1-4\rho_{33})\cos^2\theta - \frac{2}{\sqrt{3}}\text{Re}\rho_{3-1}\sin^2\theta\cos 2\phi - \frac{2}{\sqrt{3}}\text{Re}\rho_{31}\sin 2\theta\cos\phi \right]$$

$\pi^+ p \rightarrow K^{*+} (890) \Sigma^+ (1385)$



METHOD OF MOMENTS

If the decay angles of a resonance are θ, ϕ the average value of any function of these angles $f(\cos\theta, \phi)$ is defined by

$$\bar{f} \equiv \int d\cos\theta \, d\phi \, W(\cos\theta, \phi) f(\cos\theta, \phi)$$

The following formulae for extracting the density matrix elements are apparent immediately

$K^{*+}(890)$:

$$\begin{aligned}\overline{\cos^2\theta} &= \frac{1}{5}(1+2\rho_{00}) \\ \overline{\sin^2\theta \cos 2\phi} &= -\frac{4}{5}\rho_{1-1} \\ \overline{\sin 2\theta \cos\phi} &= \frac{-4\sqrt{2}}{5} \operatorname{Re}\rho_{10}\end{aligned}$$

$\Sigma^+(1385)$:

$$\begin{aligned}\overline{\cos^2\theta} &= \frac{1}{15}(7-8\rho_{33}) \\ \overline{\sin^2\theta \cos 2\phi} &= \frac{-8}{5\sqrt{3}} \operatorname{Re}\rho_{3-1} \\ \overline{\sin 2\theta \cos\phi} &= \frac{-8}{5\sqrt{3}} \operatorname{Re}\rho_{31}\end{aligned}$$

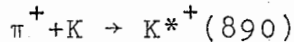
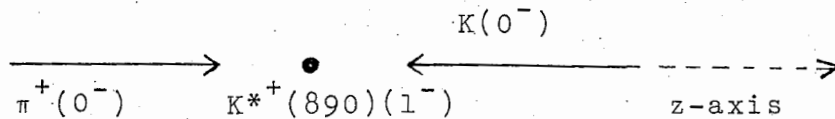
In the method of moments we use approximations of the form

$$\overline{\cos^2\theta} = \frac{1}{N} \sum_b \cos^2\theta_b \quad \begin{array}{l} \theta_b = \text{experimentally observed} \\ \text{decay angle} \end{array}$$

and utilize the formulae above to calculate the matrix elements, The approximation is better the more events we have.

PARTICLE EXCHANGE PREDICTIONS

By considering conservation of spin, parity and strangeness at each production vertex it is easy to conclude that the exchanged particle must be either K or K*. On simple considerations of parity conservation and angular-momentum coupling we can predict values for some of the matrix elements for each exchange at each vertex. As an example take K exchange at the K*⁺(890) vertex.



Conservation of parity and angular momentum implies $\ell = 1$ ($\ell_z = 0$ along the direction of incident particle). Therefore

$$\langle m = \pm 1 | 4_J \rangle = 0$$

therefore

$$\rho_{\pm 1 m}^{K^*} = 0$$

Other predictions follow similar reasoning (Schmitz (1965))

On page 64 we list the density matrix elements for this experiment along with those at other energies. There is

agreement on the matrix elements at different energies but neither K^* nor K exchange is consistent with the experimental values.

Form factors and models incorporating absorption of some of the partial waves have been used in an attempt to get better agreement with experiment (Schmitz 1965). For some reactions these work quite well but in our case the results are not substantially better (Toet 1974).

QUARK MODEL PREDICTIONS

On the basis of the quark model the following relations between the baryon and meson density matrix elements in this reaction are predicted (Bialas 1968).

$$\rho_{11} = \frac{1}{2}(1 - \rho_{00}) = \frac{3}{4}\rho_{33}$$

$$\rho_{1-1} = \frac{4}{\sqrt{3}}\rho_{3-1}$$

$$\rho_{10} = \frac{4}{\sqrt{6}}\rho_{31}$$

From our data we find

$$\rho_{11} - \frac{3}{4}\rho_{33} = 0.14 \pm 0.07$$

$$\rho_{1-1} - \frac{4}{\sqrt{3}}\rho_{3-1} = -0.02 \pm 0.18$$

$$\rho_{10} - \frac{4}{\sqrt{6}}\rho_{31} = 0.14 \pm 0.12$$

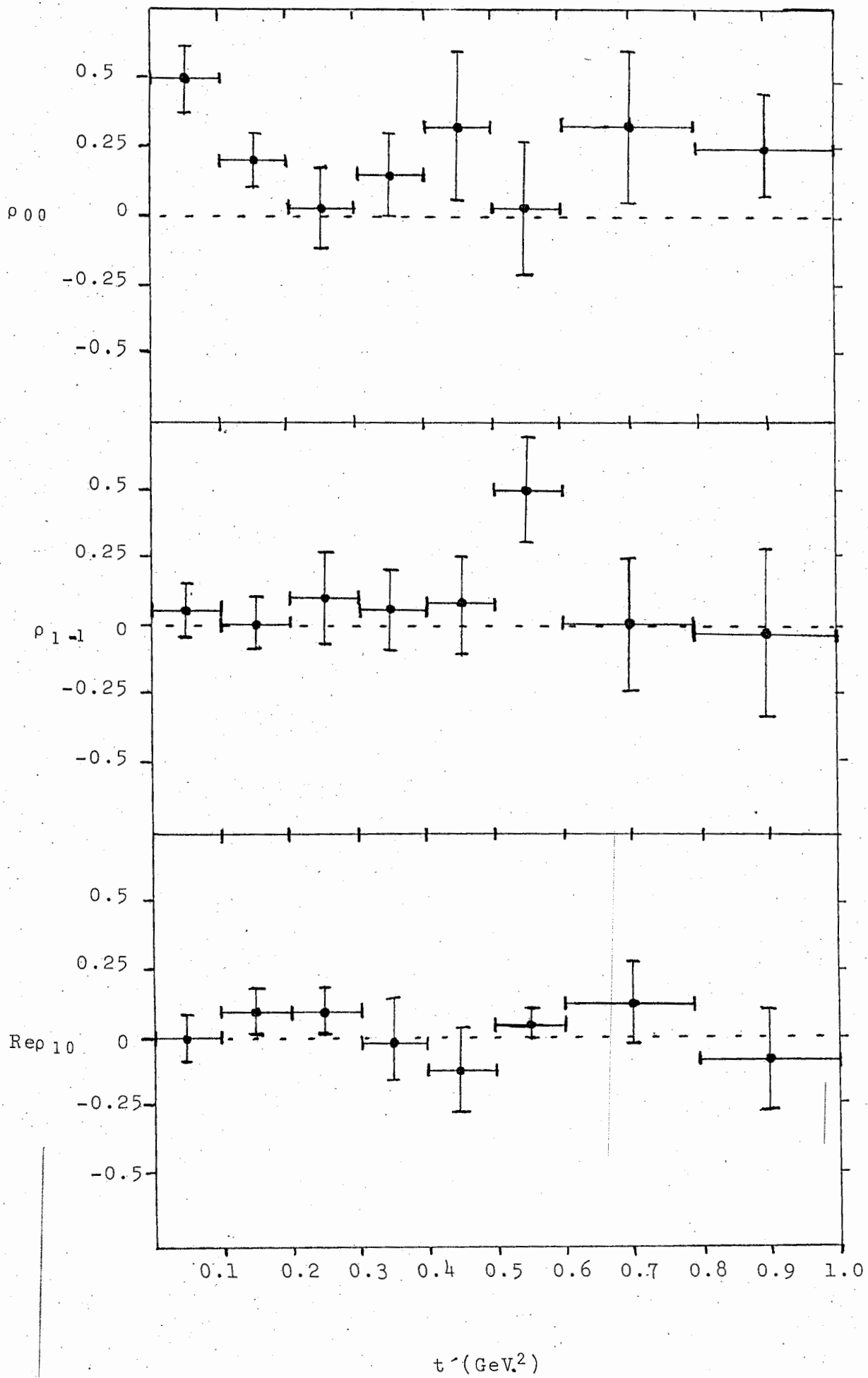
The agreement is reasonable.

SLOPE PARAMETER OF THE DIFFERENTIAL CROSS SECTION FOR $\pi^+ p \rightarrow K^{*+}(890) \Sigma^+(1385)$

p_{beam} GeV/c	t' region GeV ²	λ (slope) GeV ⁻²	ref.
4.0	< 2.0	1.7 ± 0.5	Bartsch (1966)
5.0	< 1.0	2.2 ± 0.8	Toet (1974)
8.0	< 1.2	1.6 ± 0.8	Aderholz (1969)
10.3	< 1.0	3.2 ± 0.3	This experiment

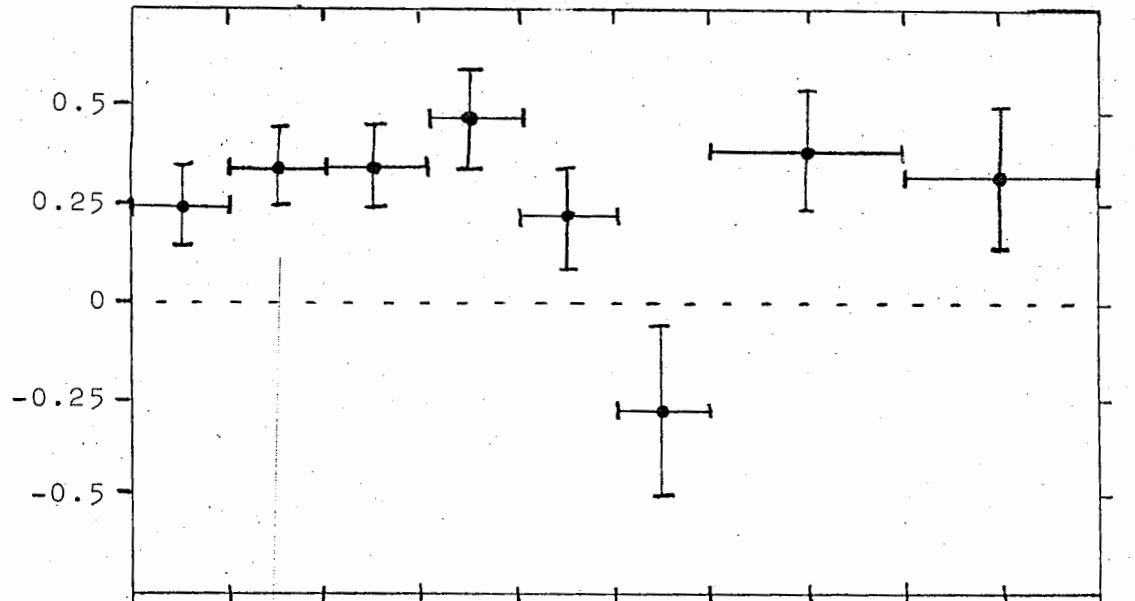
SPIN DENSITY MATRIX ELEMENTS FOR $\pi^+ p \rightarrow K^{*+}(890) \Sigma^+(1385)$

p_{beam} (GeV/c)	ρ_{00}	$\rho_{1,-1}$	Re $\rho_{1,0}$	$\rho_{3,3}$	Re $\rho_{3,-1}$	Re $\rho_{3,1}$	Ref.
3.7	0.32 ± 0.08	0.08 ± 0.06	-0.09 ± 0.05	0.20 ± 0.06	-0.04 ± 0.06	-0.12 ± 0.07	Butler (1973)
5.0	0.40 ± 0.14	0.02 ± 0.11	0.02 ± 0.07	0.18 ± 0.09	0.09 ± 0.10	0.01 ± 0.11	Toet (1974)
5.5	0.18 ± 0.10	-0.11 ± 0.09	-0.06 ± 0.06	0.19 ± 0.09	0.12 ± 0.07	-0.09 ± 0.08	Cooper (1970)
8.0	0.28 ± 0.13	-	-	0.30 ± 0.08	-	-	Aderholz (1969)
10.3	0.26 ± 0.06	0.07 ± 0.06	0.04 ± 0.04	0.30 ± 0.05	0.04 ± 0.05	-0.06 ± 0.05	This exp.
K exchange	1	0	0	0	0	0	Schmitz (1965)
K* exchange	0	arbitrary	0	0.375	0.216	0	Sakurai (1963)

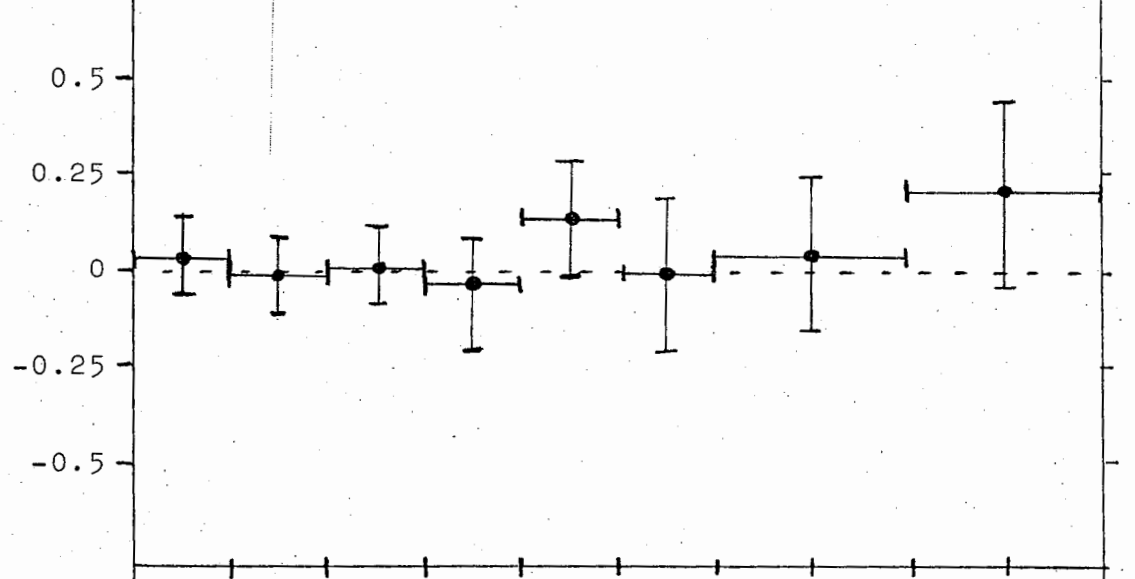


Z(385) Density Matrix Elements as functions of t

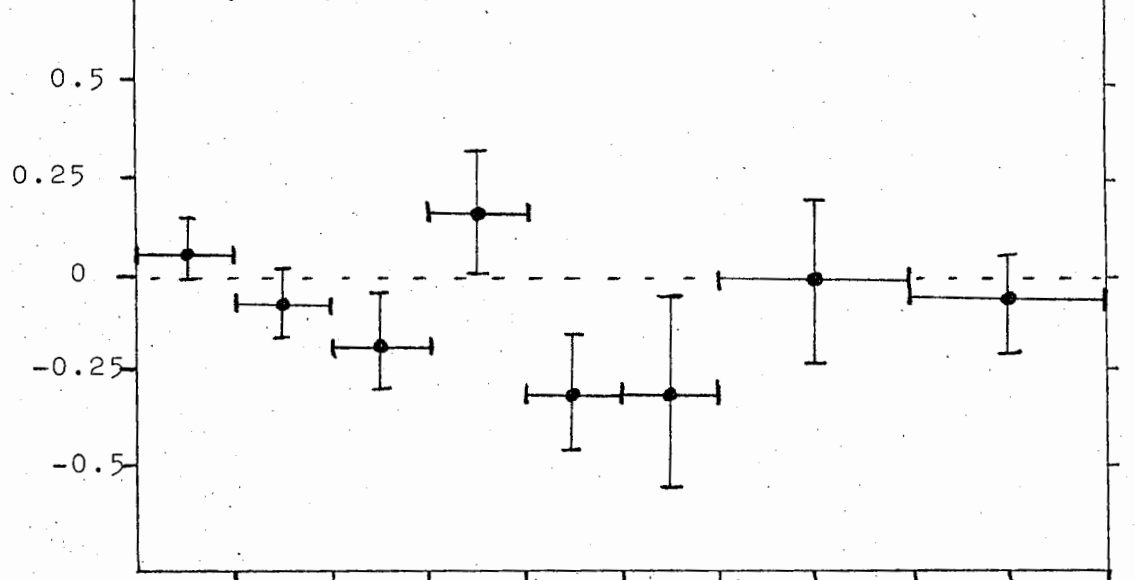
ρ_{33}



$\text{Re}\rho_{3-1}$



$\text{Re}\rho_{31}$



t (GeV²)

References

- Aderholz, M., et. al., Nucl. Phys. B11, 259 (1969)
- Bartsch, J., et. al., Nuovo Cimento 43, 1010 (1966).
- Berge, J., Solmitz, F., Taft, H., Rev. Sci. Instr. 32 538 (1961).
- Bialas, A., Zalewski, K., Nuclear Physics B6, 465 (1968).
- Bock, R., Application of a generalised method of least squares for Kinematic Analysis of tracks in Bubble Chambers (CERN 60-30, 1960).
- Bradner, M., Bubble Chambers, Ann. Rev. Nucl. Sc., 10, 109 (1960).
- Butler, W., et. al., Physical Review D7, 3177 (1973).
- Cobb, Magnetic Field of the SLAC 82-inch Hydrogen Bubble Chamber at 4808 Amps. (LRL 663, 1968).
- Cooper, W., et. al., Nuclear Physics B23, 605 (1970).
- Crennell, SLAC 82-inch Hydrogen Bubble Chamber Optical Constants (BNL 14780, 1970).
- Dahl, O., et. al. Squaw Kinematic Fitting Program (Berkeley P-126 (1968).
- Davis, P., Density and Range Momentum Table for Liquid Hydrogen in the 82-inch Chamber (LRL 656, 1968).
- Flatte', S., Beam Averaging for the SLAC C-K Beam (LRL 664, (196
- Flatte', S., Manual for K82 Beam Watchers (LRL 646, 1968).
- Flatte', S., et. al., 82-inch Bubble Chamber Optics Calibration (LRL 658, 1968).

Flatte', S., et. al., Magnetic Field of the SLAC 82-inch Hydrogen Bubble Chamber at 4808 Amps (LRL 773, 1968).
Gottfried K., Jackson J., Nuovo Cimento 33 309 (1964).
Henderson, Cloud and Bubble Chambers, (Barnes and Noble, 1970).
Khoury, B., U of Maryland Technical Report 73-944 (1972).
LRL Detectors, the 72-inch Bubble Chamber, (Berkeley, 1963).
Nishijima, K., Progr. Theor. Physics 12 107 (1954).
Particle Properties, Physics Letters 50B 1 (April 1974).
Rosenfeld, A., Humphrey, W., Analysis of Bubble Chamber Data, Ann. Rev. Nucl. Sci. 13 103 (1963).
Sakurai, J., Stodolsky, R., et. al., Phys. Rev. Lett. 11, 90 (1963).
Schmitz, Peripheral Collisions, Cern Easter School 1965 Vol. 1 SLAC users Handbook, Stanford University, California.
Solmitz, F., Johnson, A., Day, T., TVGP Program (Berkeley P-117) (1965).
Toet, Strange Particle Production in 5 GeV./c π^+ p Collisions (1974).
Zoll, J., (1965).